https://doi.org/10.5194/egusphere-2026-3826
Preprint. Discussion started: 17 August 2026


# A drone-based method for simultaneous flux measurements of multiple greenhouse gases at hectare-scale with in-flight calibration and tracer gas release

Magnus Gålfalk[1], Henrique Sawakuchi[1], Guillem Domènech-Gil[1], Åsa Kasimir[2], David Bastviken[1]

[1]Department of Thematic Studies – Environmental Change, Linköping University, 58183 Linköping, Sweden
[2]Department of Earth Sciences, Gothenburg University, Box 460, 40530 Gothenburg, Sweden

*Correspondence to*: Magnus Gålfalk (magnus.galfalk@liu.se)

**Abstract.** Convenient in situ methods are key for detecting, quantifying, and mitigating gas emissions. Uncrewed aerial vehicles (UAVs), comprising drones equipped with lightweight integrated instruments, offer a promising platform for mapping greenhouse gas (GHG) emissions. However, flux area attribution can be challenging, and the low-weight gas analyzers or sensors required for drones may exhibit drift over time that degrades detection limits and increases measurement uncertainty.

We have developed a UAS (uncrewed aerial system) based approach with all instrumentation onboard, mapping gases, here focusing on simultaneous measurements of the GHGs methane ($CH_4$), carbon dioxide ($CO_2$), nitrous oxide ($N_2O$), and ethane ($C_2H_6$). The key innovations are the combination of onboard multi-gas measurements, in-flight drift correction using onboard reference air, and integration of controlled tracer gas ($C_2H_6$) release to constrain the area attribution of detected fluxes. We explore four different flight patterns (box, two-wall, long wall, and 2D-mapping), each suited to different measurement scenarios, and demonstrate their application in diverse environments, including a rewetted peatland, the littoral zone of a lake, manure wells, and a barn housing dairy cows. Our results show the importance of in-flight drift correction or drift control, and that this can reduce baseline-related uncertainty of UAS-based mass balance approaches, which can be key for improving detection limits and estimation of GHG fluxes in a wide range of environments and settings. Furthermore, combining tracer gas emissions with drone flights aids in separation of sources in the area of interest, verification that targeted emissions are intercepted by the sampling walls, and determination of the upper integration height needed to capture source-related transport.

## 1 Introduction

Decreasing greenhouse gas (GHG) emissions is key for future generations. Consequently, most countries have agreed to reduce GHG emissions through international agreements, including the United Nations (UN) Paris agreement. Transparency and accountability fundamentally rely on the coordinated National Greenhouse Gas Inventories Programme (NGGIP) (IPCC

https://doi.org/10.5194/egusphere-2026-3826
Preprint. Discussion started: 17 August 2026


2006, and its later refinements). A successful implementation of the NGGIP fundamentally requires that reported GHG emissions are accurate and that nations have the capacity to identify their GHG emissions and verify that they mitigate them efficiently. Unfortunately, convenient local capacity for measuring GHG emissions remains limited, and several studies have revealed substantially biased emissions using the NGGIP emission factor modeling approach compared with on-site flux measurements. A synthesis of methane ($CH_4$) emissions from the US oil and natural gas systems showed that fluxes from field measurements were 1.5 to 2-fold greater than NGGIP estimates (Alvarez et al., 2018; Rutherford et al., 2021). Furthermore, disproportionally large emissions have been found from low-production oil and natural gas production sites, which are not detected as ultra-emitters by remote sensing (Lauvaux et al., 2022). These findings highlight the need for improved approaches to identify and eliminate leakages from such facilities (Omara et al., 2022). The International Energy Agency (IEA) Global Methane Tracker also indicates that energy sector $CH_4$ emissions are 70% higher than officially reported (IEA, 2022). Likewise, $CH_4$ emissions from agricultural ponds seem underestimated by the NGGIP (Malerba et al., 2022). New and large previously unrecognized anthropogenic $CH_4$ and nitrous oxide ($N_2O$) fluxes from wastewater treatment (e.g. Gålfalk et al. 2022; Gålfalk and Bastviken 2025) have been observed and extensive measurements of US wastewater treatment plant emissions yielded fluxes that were 1.9 times greater than the NGGIP estimate reported (Moore et al., 2023). Furthermore, distributed emissions across landscapes, including the efforts towards nature-based solutions to increase landscape carbon sinks by e.g. rewetting of drained peatland are poorly constrained (Escobar et al., 2022). In addition, it is now clear that land use or climate change are shaping many of the fluxes traditionally thought of as natural (Bastviken and Johnson, 2025; Koffi et al., 2020; Wang et al., 2026), eroding the distinction between natural and anthropogenic GHG fluxes. All these findings highlight the importance of effective GHG monitoring capacity for all types of environments.

A reason for the biased NGGIP flux estimates is the absence of comprehensive monitoring and a scarcity of methods for cost-effective measurements of local GHG fluxes. To identify and mitigate local emissions from facilities and in landscapes, affordable and effective approaches are required that can be routinely applied by managers. A recent survey of GHG flux methods highlighted the challenges to accurately assess scales from $m^2$ to tens of hectares, representing the typical scales of facilities and land-use activities (Bastviken et al., 2022). Measurements at this scale are therefore key for setting effective priorities and verifying flux reduction efforts. To be widely useful, measurement methods should be non-invasive (i.e. do not disturb the target area), mobile, and capable of integrating fluxes over areas of interest while having a well-constrained target area (sometimes referred to as flux footprint). This generates a need to explore alternatives to traditional flux chamber and eddy covariance approaches (Bastviken et al., 2022).

Recent progress in facility-scale GHG flux measurements includes satellite remote sensing for mega-emitter facilities (Lauvaux et al., 2022). There has been rapid development in the remote sensing domain, with multiple ongoing or planned missions to map GHG sources (Wang et al., 2023). However, far from all emissions can be detected from space, as many are

https://doi.org/10.5194/egusphere-2026-3826
Preprint. Discussion started: 17 August 2026


below the detection limits of current satellites and supplementary near-ground methods are therefore needed (Bastviken et al., 2022; Omara et al., 2022). Hyperspectral infrared (IR) gas imaging is one alternative and, under suitable conditions, has revealed and quantified previously unknown large $CH_4$ and $N_2O$ emissions from biogas facilities, biofertilizer storage, $CH_4$ flaring, and from wastewater treatment plants (Gålfalk et al., 2022; Gålfalk and Bastviken, 2025).

Another alternative is the use of drone-borne measurement systems, which have been highlighted as one of the most promising new GHG assessment approaches (Corbett and Smith, 2022; Hollenbeck et al., 2021; Jońca et al., 2022; Olaguer et al., 2022). UAS GHG methods have the advantage of being able to sample data over large areas in a short time and in complex environments, but payload limitations often restrict the use of laboratory-grade instruments and the number of instruments that can be carried. To achieve greater sensitivity, onboard co-located and simultaneous measurements of GHG concentration, wind speed, and wind direction (/independent of any instruments on the ground) have been proposed (Gålfalk et al., 2021). Examples of such independent UAS GHG flux measurements (iUAS-$F_{GHG}$) are still limited (Bolek et al., 2024; Gålfalk and Bastviken, 2025; Jońca et al., 2022; Scheutz et al., 2025). Previous efforts have highlighted the need for several improvements, including:

(i) Sensor drift issues need to be reduced to achieve lower detection limits. Drifts in gas concentrations of analyzers and sensors on a UAV can be considerable and nonlinear, and stabilization can take several hours if at all reached within reasonable time (exemplified in results later). In our experience, drift can be substantial after liftoff, even following extended stabilization on the ground. This is mainly due to temperature drift in the gas analyzer, as it is cooled by increased surrounding airflow (e.g. downwash from the UAV's propellers) and by changes in meteorological variables during flight.

(ii) Constraining air movements across a target area at the time of flight is important for flux assessment given complex surface roughness and wind variability (e.g. Bolek, Heimann, and Göckede 2024).

(iii) Measuring $CH_4$, $CO_2$, and $N_2O$ simultaneously for the same target areas using iUAS-$F_{GHG}$ would be highly beneficial for comprehensive GHG assessments and does not appear to have been done to date.

Inspired by these challenges, we here extended the previous iUAS-$F_{GHG}$ approach (Gålfalk et al., 2021; Gålfalk and Bastviken, 2025) with capacity for simultaneous measurements of multiple GHGs, adding in-flight drift correction of GHG instruments, and constraining air movement assessments using simultaneous tracer gas measurements. This method development makes it possible to reach detection levels well below those previously shown from e.g. waste facility emissions, enabling assessment of some natural landscape emissions. We provide examples from contexts relevant to farms (agriculture), lakes, and wetlands using flight patterns suitable for different wind conditions.

https://doi.org/10.5194/egusphere-2026-3826
Preprint. Discussion started: 17 August 2026


## 2 Methods

### 2.1 Equipment and general information

The iUAS used was an Airolit XLT (Airolit AB) with a payload capacity of 5 kg, equipped with two Aeris Strato gas analyzers ($CH_4/C_2H_6$ and $N_2O/CO_2$; Aeris Technologies) weighing 1.9 kg each, a 2D-anemometer (LI-550 TriSonica Mini, LI-COR) mounted on an extendable pole on top of the drone (anemometer-propeller distance of 94 cm, corresponding to 1.54 rotor diameters, which was enough to minimize disturbances (Moormann et al. 2025; also verified vs stationary reference anemometers in situ), and small auxiliary sensors (Sparv SKS1 sensor for air temperature and relative humidity; two SKP sensors for air pressure); all connected to a logger (SKH3, Sparv Embedded AB) sampling and synchronizing data at 1 Hz. The system was integrated by Sparv Embedded AB.

The iUAS was equipped with a gas bag (FlexFoil Sample Bag 10 L) holding reference air (filled with outside air before each flight) for periodic in-flight drift correction (Fig. 1) and a remote-controlled valve to switch between outside air and reference gas manually using the drone remote controller. Outside air is drawn from a gas inlet close to the anemometer in order to measure wind and gas concentrations at the same point. We were close to the maximum payload of 5 kg typically allowing flight times of about 25 minutes (depending on wind and drone speed). The drone was flown manually within sight in all environments for safety reasons, as minimum flight altitudes were often only one meter above ground level, and GPS altitude estimates can drift up to several meters during a flight. The pump speed voltage of both Aeris sensors were set to 4.95 V (maximum value) to minimize the time delay between air entering the gas inlet and measurements being made, and the time needed to replace air completely in the gas cell.

Flight speeds represented a compromise between flying slow enough to adequately sample each altitude with sufficient horizontal resolution, and yet fast enough to cover reasonably large areas, and preferably only sampling reference air when changing flight direction (such as the end points of wall flights while going to the next altitude). In most cases, this translated to flying with a speed of 2-5 m/s, with the flight speed kept as constant as possible during each flight.

https://doi.org/10.5194/egusphere-2026-3826
Preprint. Discussion started: 17 August 2026


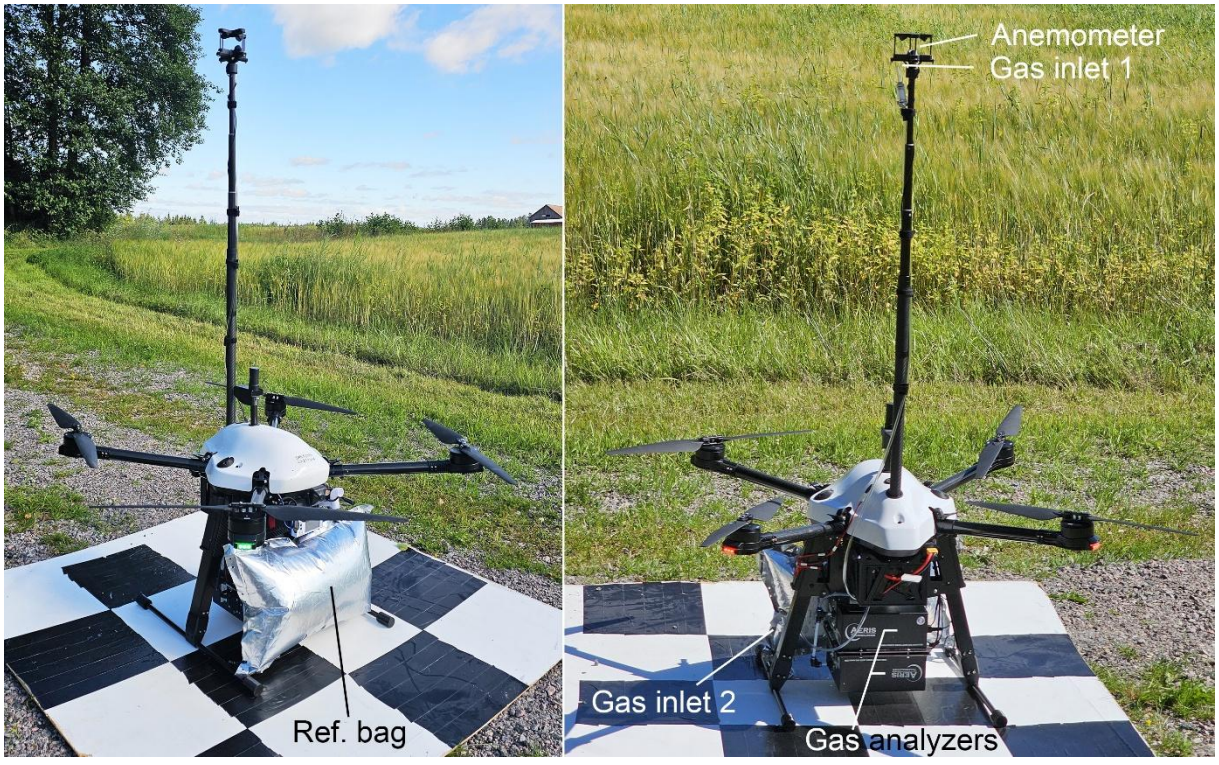


**Figure 1.** Our iUAS system consisted of an anemometer on an extendable pole, two optical Aeris trace gas analyzers ($CH_4$+$C_2H_6$ and $CO_2$+$N_2O$), auxiliary sensors (air temperature, humidity, and pressure), a logger, and a reference gas bag used for in-flight drift correction of the gas analyzers. The two gas inlets (outside air and reference bag air) are marked in the right panel.

## 2.2 Instrument drift correction

One aim was to enable reasonably simple drift correction of gas concentrations which is a challenge especially for drone-based systems that due to payload limitations often require low-weight instruments. Some low-weight instruments show larger drifts (examples given later) which could be due to temperature-stable measurement cells being more difficult to design for low-weight instruments. Such a drift is especially important to correct for when measuring fluxes in natural landscapes, where concentration gradients are typically much lower than where anthropogenic point-source emissions dominate.

To enable tracer-verified, in-flight drift correction, gas from the reference bag was periodically sampled at selected times during flights to allow instrument drift correction in post-processing. Because the gas analyzers were calibrated to reference gas standards regularly in the laboratory, the in-flight drift correction focused on relative calibration versus a constant reference gas resembling the sampled air in terms of trace constituents. We therefore used ambient air pumped into the gas

https://doi.org/10.5194/egusphere-2026-3826
Preprint. Discussion started: 17 August 2026


bag before each flight. The drift-correction was done in post-processing using measurement points of the reference gas (which had a constant concentration during the whole flight) by fitting them with a spline curve and correcting the baseline of the outside air data. Our best results were found by using reference gas close to ambient levels (typical outside air before a flight), with care taken not to breathe or emit tracer ethane ($C_2H_6$) gas while filling the reference gas bag before each flight. The response times of changes in gas concentrations, for both gas analyzers, with regards to the inlet at the anemometer were routinely checked and are considered in the calculations (the time delay between gas intake and change in measured gas concentrations; about 2 s with a pump voltage of 4.95 V for both analyzers). The response time for collecting reference bag data is shorter as the tube connecting the bag and the analyzers is shorter.

Some important considerations that need to be taken into account are 1) the number of reference gas samples that are needed and can be done during a single flight, limited by the volume of the gas bag; 2) the maximum time-interval that can be used between drift corrections for all gases; and 3) the loss of total effective flight time for outside-air sampling due to sampling of reference gas bag air. Likewise, the frequency of reference gas measurements during flights determines the time between baseline drift calibration points. This influences the accuracy of the corrections, as the reference gas measurements need to have at least twice the frequency of the baseline drift (Nyquist-Shannon sampling theorem). Hence, we also performed tests on how different reference gas measurement frequencies influenced baseline correction. This was done by hovering at high altitude (100 m) in well-mixed air and changing how often air was sampled from the gas bag, followed by a test flying repeated vertical profiles between 0-120 m to compare raw and drift-corrected concentrations.

### 2.3 Tracer gas release and air movement patterns

Another aim was to address the challenge of determining the dispersion and vertical movement of emitted gas from different parts of the target area – in turn affecting the optimization of what flight tracks to consider for the most accurate assessments of a target area. For example, if gas from the target area only influences concentrations and mass transport up to a maximum of 30 m altitude, the consideration of air up to 120 m in the flux calculations would add irrelevant noise that only increases uncertainty (especially since higher altitudes usually mean stronger winds, increasing the impact of higher altitudes on vertical flux density profiles). In an optimized evaluation of mass transport only altitudes which are relevant for the target area fluxes should be included in the flight paths. It is therefore beneficial to understand the air movement patterns determining dispersion and vertical rise. Air movement models for this are sensitive to the in-situ variability in topography, surface roughness, wind shadows, air heating, etc., or are computationally very expensive and not adapted for all landscapes. Therefore, in-situ verification of air movement is beneficial. The release of a separate detectable tracer gas helps provide the desired information. Further, given short-term variability in wind speed and direction during flights it is beneficial to have a tracer gas to constrain how well the drone measurements capture a known flux within the target area.

https://doi.org/10.5194/egusphere-2026-3826
Preprint. Discussion started: 17 August 2026


Tracer experiments were done using $C_2H_6$ placed strategically in or at an edge of a target area. We used a tracer release rate in the range 2-3 liters of $C_2H_6$ per minute. This was done by timing how quickly a water-filled 0.5-liter bottle held upside-down were filled with the released $C_2H_6$ and adjusting the regulator setting until filling the bottle took 10-15 seconds (noting the exact time). The tracer gas was released at ground level via a tube ending under water at air temperature in a bucket. This purging reduced the initial velocity, distributed the gas emission across the bucket area, and adjusted the temperature of the released gas to better simulate ground level emissions (compared to a very small high-velocity outlet directly from the tube). We tested tracer releases 1) next to or between potential source areas to facilitate separation of their contributions, 2) at the upwind border of a target area to constrain how much the emissions from the target area could rise before reaching the downwind wall, and 3) at the center of a target area in variable low-wind conditions combined with box flights to map where emissions from the target area leaves an enclosed area.

Examples of environments where the tracer gas method is useful are natural environments with mixed habitat types, agricultural settings or industrial environments (such as storage tanks or process steps) representing environments with strong wind shear enhanced mechanical turbulence due to complex ground structures, and during variable or low-wind conditions where the upwind and downwind directions varies during a flight.

### 2.4 Flight patterns

Flights were done in wind conditions ranging from no wind to 8 m/s average wind speed (gusts above 10 m/s). We focused on assessing mass transport of gases into and out of a selected target area according the modified mass difference method (MMD), across a flight wall by the integrated horizontal flux method (IHF), or if no wind, tested the capacity to resolve concentration gradients to be used in the nocturnal boundary layer approach (NBL) (Harper et al., 2011). The mobility and flexibility of a drone-based system greatly facilitated all of these approaches that historically have been difficult to realize given their data needs. Flight patterns providing such information (illustrated in Fig. 2), include box flights or two-wall flights (for MMD), long-wall flights (for IHF), and low-altitude 2D-mapping flights (enables NBL if successful and extended to 3D by mapping at multiple altitudes).

https://doi.org/10.5194/egusphere-2026-3826
Preprint. Discussion started: 17 August 2026


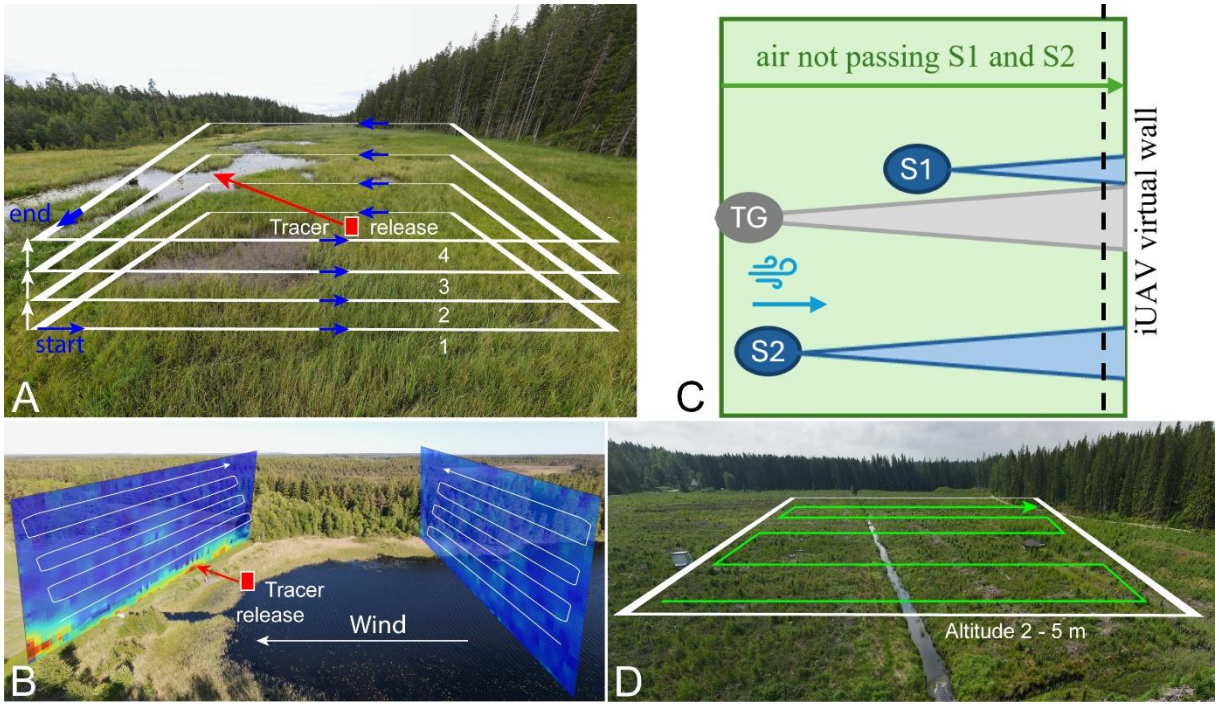


**Figure 2.** Illustration of the four different flight paths typically used in our measurements. Box flight with tracer (A), two-wall flight with tracer (B), long-wall flight illustrating two expected GHG sources S1 and S2, and trace gas TG positioned in between (C), and 2D-mapping at low altitude in wind-still conditions (D). Box and wall flights always start at the lowest altitude and move successively upwards after each altitude is finished as air below the drone will be affected by the propeller downwash. Note that indicated altitudes are illustrations, in practice the number of altitudes varies among cases and conditions.

**Box flights** means that the target area is surrounded by vertical flight walls consisting of horizontal flight lines at increasing altitudes from as close to the ground as possible and upwards. This strategy also includes "cylindrical flights" similar to what is sometimes done by aircraft measurements across larger regions (Basso et al., 2021; Gatti et al., 2021). Ideally, all four walls around a target area should be sampled in one flight to minimize the time between up and downwind measurements as wind conditions and emissions can change fast. In the examples provided here, each altitude was flown in a square or rectangular pattern (Fig. 2A), with reference gas sampled for drift correction either once per altitude level, once every other corner, or every corner, depending on the size of the box and the flight speed (adapted for the drift correction to be frequent enough). The box (or cylinder) pattern is advantageous in cases where the wind speed is low to medium as the wind direction can change frequently and every measurement point (1 Hz) includes the wind speed and direction. Under such variable wind directions, the tracer gas helps constrain how the air moves across the flight-wall point cloud at different times and altitudes.

https://doi.org/10.5194/egusphere-2026-3826
Preprint. Discussion started: 17 August 2026


**Wall flights** can be seen as a simplified version of the box flight that can cover larger areas or more altitudes in the same flight time. The typical "two-wall case" consists of flying two walls perpendicular to the average wind direction (one for incoming and one for outgoing air from a target area) and using mass balance to calculate the emission or uptake (Fig. 2B). Ideally, there should be a stable wind direction, and the area of interest should be narrower than the wall lengths to minimize the amount of gas from the target area that is lost sideways (and thereby would bypass the downwind wall). Landscape wind channeling, forcing the wind in one direction, and/or tracer gas analyses help constrain such cases. Each wall is made by flying back and forth between two GPS-coordinates, with different altitudes each pass, starting from the lowest safe level and continuing upwards as the air underneath the drone will be affected by downwash from the drone's propellers. Reference bag sampling is done at the start, at the end, and every time the drone changes altitude. An example for flying a 50 m high wall could be altitudes of 2, 4, 7, 10, 15, 20, 25, 30, 40, 50 m (resulting in 11 in-flight bag samples for drift correction). Depending on the maximum height and vertical resolution of a wall, one or two batteries can be required to sample both walls, assuming a steady state condition for the wind field during this time.

An alternative wall flight is the single **long-wall** case (Fig. 2C) flown downwind of the area of interest. The strategy with this flight pattern is to make the wall long enough to, with high certainty, allow separation of air passing the area of interest and air passing to the side of the area. This allows assessing the added or removed GHGs by the target area relative to the air not passing the target area. For cases with medium-to-strong emissions sources, which is often the case for facilities and/or plumes from spatially distinct sources, absolute fluxes can be calculated relative to the background level on the wall where air has not been influenced by the area of interest. For more extended and lower emissions, which is often the case for natural emissions, relative fluxes can be calculated by comparisons between different areas on the long wall representing air passing different land use.

For strong sources yielding concentrations clearly above the background level (e.g. gas plumes) tracer gas measurements may not be needed. For all wall flights, if several batteries are used, it is not enough to only correct for instrument drift in a relative way during each separate flight. It is important to also correct for drift between flights, which in this case was done using the assumption that concentrations at high altitudes (e.g. 100-120 m) should be the same for consecutive flights at high altitudes where the air was presumably well mixed.

Finally, **low-altitude 2D-mapping** is an alternative during stable near-ground atmospheric conditions with negligible wind speed, leading to gas accumulation over time. This is common e.g. at nighttime when cooling generates local inversions in landscape depressions. Hence, mapping 2D or 3D gas accumulation e.g. during early mornings offers a way to assess nighttime GHG exchange in some areas from the time the wind settled. In the example provided here, we demonstrate a first simplified version of such mapping, to show concentration gradients between accumulation in some areas and depletion in other areas reflecting emission, consumption, and density driven gas flows along slopes as discussed separately. By flying at

https://doi.org/10.5194/egusphere-2026-3826
Preprint. Discussion started: 17 August 2026


very low altitude, in our case 2-5 m, and at a drone speed of 3-5 m/s it was possible to cover a large area using many transects with enough space between the transects (on average 80 m) not to affect each other from propeller downwash. In-flight reference bag sampling was done between each transect. Under nocturnal inversion conditions and with little or no advection, gas emitted from the target area, representing a low point in the landscape, accumulates near the ground.

The above flight patterns are all exemplified in this study, with results presented in section 3.2. followed by a method discussion in section 3.3.

### 2.5 Flux calculation and error estimation

As a first step, using the lab-calibrated and reference bag drift corrected point cloud data of $CH_4$, $N_2O$, $CO_2$, and $C_2H_6$, we built wall maps of gas concentrations with a 1x1 m spatial resolution. Signal-to-noise is improved by calculating a moving average of three data points, and calculating averages of points that are within half a cell size (0.5 m) of each other (e.g. nearby data points in altitude or horizontally for low drone speeds such as the end parts of walls, or repeated flights), which also helps clean up point clouds before interpolation onto wall grids as this reduces the risk of introducing artifact spatial gradients at too high spatial resolution.

The same is done for wind speeds for the same data points but converting measured wind speeds and directions as measured by the drone system to become relative to the ground. This includes correcting measured wind data for the drone speed, direction, and orientation relative to north. This wind data is then mapped onto the walls of the flight pattern to yield wind speeds perpendicular to these walls. This data is treated the same way as the gas concentrations, with a 3-5 data point moving average followed by a 0.5 m proximity average filter.

For all walls, the gas concentration and perpendicular wind speed data are then interpolated into wall maps of 1x1 m spatial resolution using spatial Kriging interpolation (Myers, 1991). We use anisotropic Kriging interpolation, which takes into account that spatial correlation can change with direction, being potentially important for drone-based data as for a typical wall flight there are many more samples horizontally along an altitude than there are altitudes (often 3-7 times more). This is done in Matlab by computing variograms in different directions from the point cloud data, fitting variogram curves in the horizontal and vertical directions, computing an anisotropy ratio, and finally apply Kriging interpolation over a grid with 1x1 m resolution that covers the wall flight path.

An important core assumption for the mass balance calculations is that the air flowing into and out of a volume must be the same (otherwise the air pressure would change). Calculations are done in altitude segments, e.g. 30 or 120 segments from 1 - 120 meters altitude, with total perpendicular wind speeds of the walls normalized so that in and outflowing air volumes are equal, while maintaining all wind variations within each segment. For box and two-wall flights, this is done in different ways, as the two-wall case can have walls of very different lengths and the box case encapsulates an area. For the two-wall

https://doi.org/10.5194/egusphere-2026-3826
Preprint. Discussion started: 17 August 2026


case we therefore normalize by surface area for the incoming and outgoing walls in each altitude segment. For the box flights this instead involves four walls (often two incoming and two outgoing) where the total incoming and outgoing air volumes are made equal by scaling total incoming and outgoing winds so that their respective sums are equal within each segment (Fig. 3A).

For each coordinate on the interpolated walls (perpendicular velocity and gas concentration matrices), representing a 1x1 m vertical area, the flux density was calculated via the common gas law to yield concentrations, deriving partial pressures from the mixing ratio measurements and converting moles of gas to grams, and multiplying with horizontal wind speed using:

$$F_g(x,y) = (M_g/R)\cdot(P_{air}/T_{air})\cdot X_g(x,y)\cdot 10^{-6}\cdot v_{wp}(x,y) \quad (1)$$

where $x$ and $y$ are the coordinates on the wall (m), $P_{air}$ and $T_{air}$ are the air pressure (Pa) and temperature (K), respectively, $X_g$ is the gas mixing ratio (ppm), $v_{wp}$ is the wind speed perpendicular to a wall ($m\cdot s^{-1}$), $M_g$ is the molar weight of the gas ($g\cdot mol^{-1}$), and R is the universal gas constant ($J\cdot K^{-1}\cdot mol^{-1}$) (Gålfalk and Bastviken, 2025). The calculated flux density $F_g$ has the unit $g\cdot m^{-2}\cdot s^{-1}$.

For two-wall and box flights, statistics related to wind speed, gas concentrations, and fluxes, are calculated using all the point measurements in each altitude segment. The net flux is then the difference between the outgoing and incoming flux densities for each segment. The total flux from the area between the walls is calculated by adding net fluxes for all segments up to an altitude limit that is high enough that all potential sources and sinks within the enclosed area can be measured at the outgoing wall. This altitude limit can be determined from the altitude range at which the ethane tracer (placed at the upwind target area border) is measured on the outgoing wall.

The flux uncertainty for the two-wall and box flight case (Fig. 3A) is calculated from a combination of Monte Carlo and bootstrapping. The Monte Carlo method, using 1000 iterations, was chosen as the flux uncertainty from mass balance is complex and depends on uncertainties of many parameters – gas concentration (± 1 ppb for $CH_4$; ± 0.35 ppb for $C_2H_6$; ± 0.2 ppb for $N_2O$; and ± 0.3 ppm $CO_2$), wind speed (± 0.2 $m\cdot s^{-1}$), wind direction (± 1°), residuals of drift correction (fit dependent – different for each flight), GPS-position (± 0.5 m), altitude (± 0.5 m), and the maximum altitude included in the mass balance (± 10%). These uncertainty ranges represent standard deviations in normal distributions, from which values were randomly sampled for each run in the Monte Carlo analysis. In addition, there is an uncertainty in how well the vertical walls are sampled which subsequently affects kriging interpolations - for this we use bootstrapping to randomly keep 90% of all data points at each altitude which is included in the Monte Carlo calculations.

https://doi.org/10.5194/egusphere-2026-3826
Preprint. Discussion started: 17 August 2026


Target areas exchanging gas on the ground are calculated from the GPS-coordinates of the walls, either from the wall distances and lengths used (two-wall case) or the enclosed area (box case). Dividing the total flux with the ground area then gives a measurement of the emission or uptake from the enclosed target area ($mg \cdot s^{-1} \cdot m^{-2}$).

For the long-wall (one wall) case (Fig. 3B), if plumes are present, which is often the case for anthropogenic emissions, fluxes of one or several plumes can be calculated relative to the background level (the average level outside plumes) by using areas of the flux wall clearly corresponding to the plumes. The flux uncertainty can in this case be calculated from flux measurements of equally large background areas on the flux wall (for areas at higher altitudes a correction can be made using the average wind speeds calculated at each altitude).

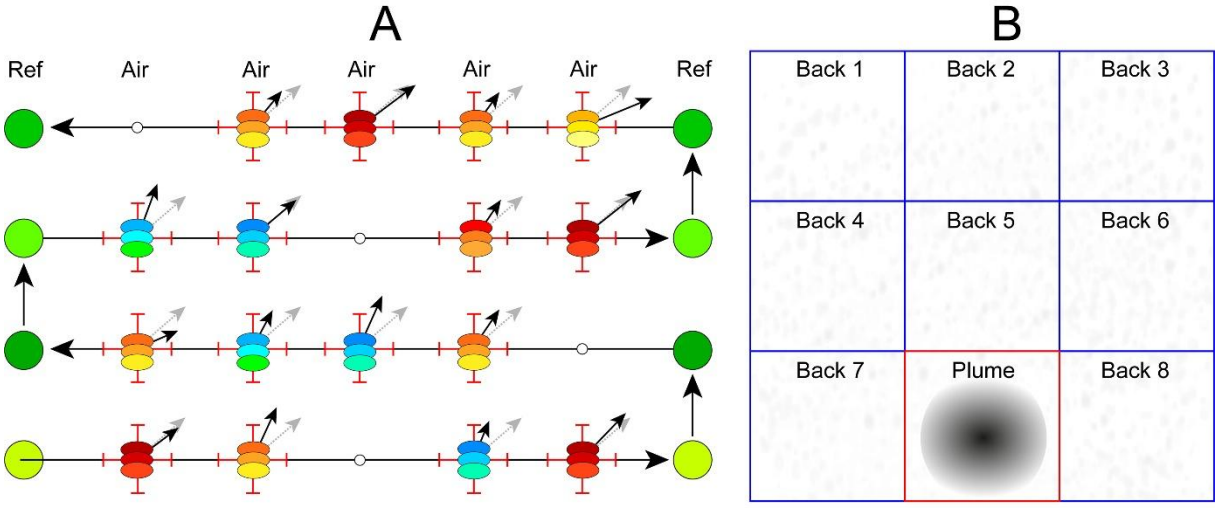


**Figure 3.** Illustration of flux uncertainty calculations for different cases. For box and two-wall flights (**A**) both Monte Carlo and bootstrapping are used to calculate fluxes for n=1000 iterations. Gray arrows illustrate measured air motion, while perturbed values for all variables listed in the above text are exemplified for air motion (black arrows), position (red crosses), gas concentration (three colors indicating uncertainty), and drift correction (large circles with colors indicating uncertainty from fit residuals between each calibration). The labels Ref and Air indicate reference bag and outside air measurements, respectively. The "empty spots" exemplify how only 90% of the data was used for each Monta Carlo run to include uncertainty of distance between measurement points and consequently also the interpolation. For a long-wall (one wall) plume case (**B**) the background areas (Back) are used to calculate (i) the average concentration outside of the plume, and (ii) the fluxes of background areas (blue squares). The plume flux is calculated from excess gas concentrations in the red square, while the flux uncertainty is estimated from the standard deviation of the background fluxes.

https://doi.org/10.5194/egusphere-2026-3826
Preprint. Discussion started: 17 August 2026


## 3 Results and discussion

### 3.1 Instrument drift correction

Regarding the response time of the gas analyzers (Aeris), a sudden concentration change (e.g. breath test; blowing in front of the gas tube for air intake) took 2 s to be noticeable by the instruments, given the length of the gas tube and the pump speed of the instruments. It took 7 s to replace air in the gas cell and for a new concentration to fully stabilize. Each bag-sampling for in-flight drift correction thus first takes 9 s to fill the gas cell with reference gas and then another 9 s to replace the reference gas with outside air. This means a total time of at least 18 s per reference bag sample.

A test to optimize the frequency of reference measurements showed that a frequency between 32 and 78 s was needed for adequate baseline drift correction (Fig. 4). This led to a routine of flying for a maximum of 60 s and calibrating for 18 s, meaning that almost 25% of the flight time was used to ensure capacity to correct the baseline and thereby increase the precision. In practice, for a wall flight, it is easier to calibrate each time the altitude is changed, which could mean more frequent drift corrections (e.g. flying 40 s and calibrating 18 s for a wall length of 200 m and a speed of 5 m/s).

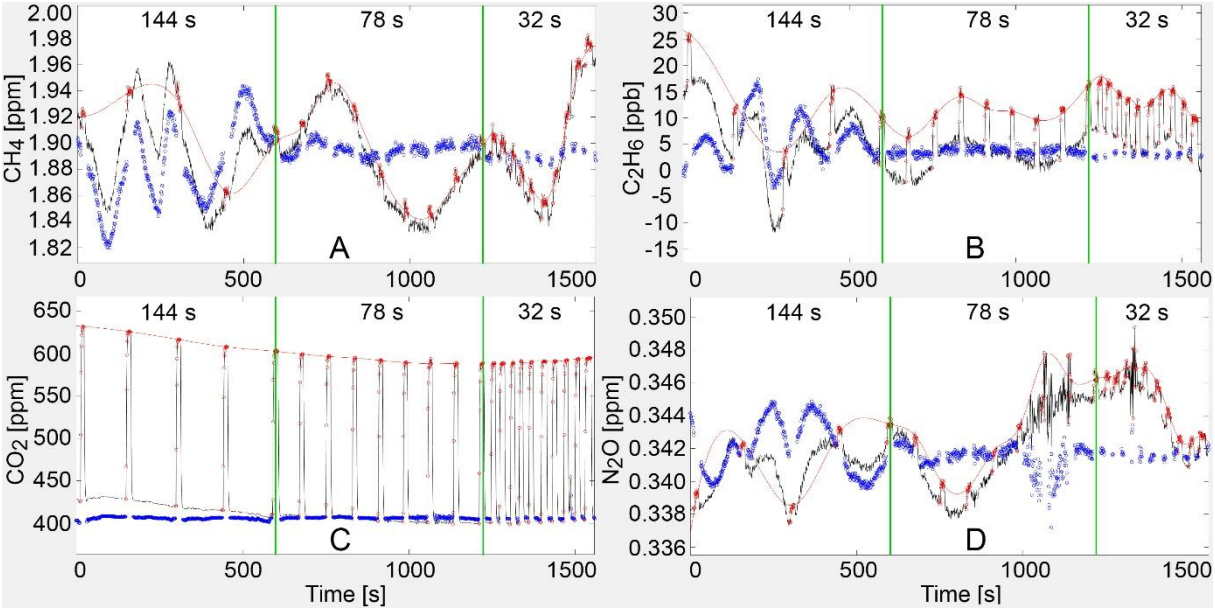


**Figure 4.** Instrument drift correction frequency test using well-mixed background levels at high altitude, showing raw (black) and calibrated (blue) concentrations of simultaneously sampled $CH_4$, $C_2H_6$, $CO_2$, and $N_2O$, respectively. Red symbols and fitted curve indicate reference points when air was measured from the on-board reference gas bag. The time between reference measurements (top of panels) was changed during the flight (144, 78, and 32 s) at times indicated by the green lines as a test of what correction frequency was needed. In this test we used reference air with $CH_4$, $C_2H_6$, and $N_2O$ close to the background level and $CO_2$ at a higher concentration (about 600 ppm). Note that the drift correction does not produce a stable blue baseline at a 144 s reference gas sampling interval, but produces much more stable baselines at 78-32 s intervals.

https://doi.org/10.5194/egusphere-2026-3826
Preprint. Discussion started: 17 August 2026


In another test we flew profiles between the ground and 120 m to include shifts in air temperature, pressure and humidity. While bag-sampling for drift corrections every 75 s was a clear improvement over corrections every 150 s for $CO_2$ (Fig. 5) which had the slowest drift, this was not the case for $CH_4$, $C_2H_6$, or $N_2O$ (Fig. 4). This has to do with the Nyquist-Shannon theorem of sampling frequency, where a signal has to be sampled at least twice its highest frequence component (otherwise the instrument drift curve fitting will miss peaks and valleys). As can be seen in Fig. 4, the drift correction might be slightly improved further for these gases if calibrating every ~30 s; however, in that case, more time is spent on drift correction than collecting environmental data (60% and 30% flight time used for reference data for 30s and 60s sampling interval, respectively) and the total flight time would be shorter as it would be limited by the amount of air in the gas bag. Thus, we have aimed for about one drift correction per minute in our further measurements.

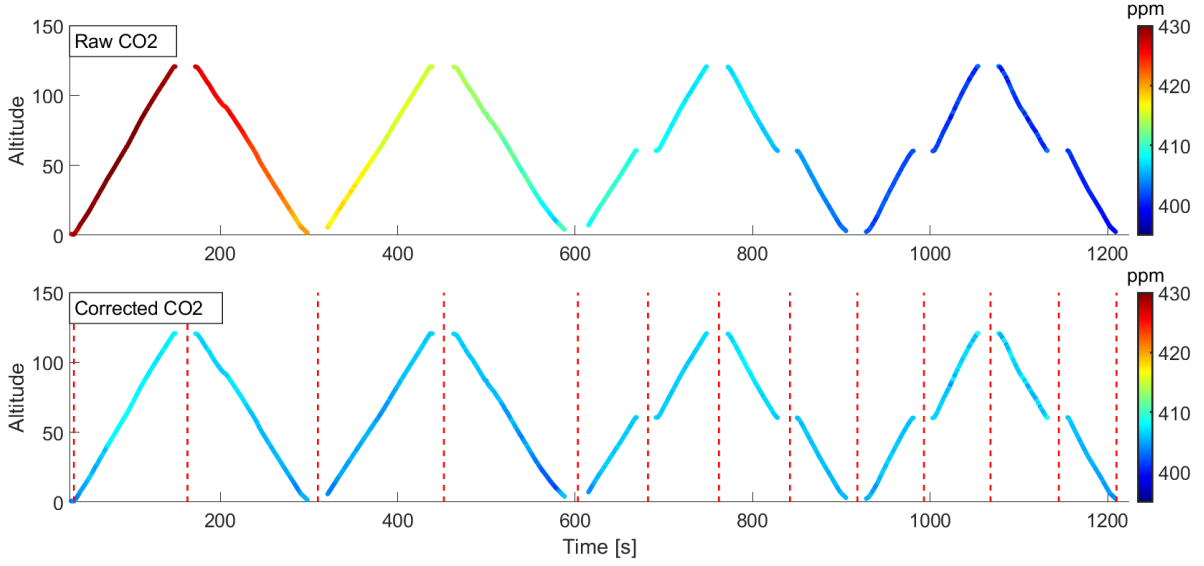


**Figure 5.** Raw and drift-corrected $CO_2$ concentrations for four vertical test profiles and at two different drift correction frequencies (every 150 s and 75 s, respectively). Vertical profiles were chosen in this test, as large changes in ambient temperature, pressure, and humidity could be a source of drift. The red dashed lines mark reference data points when the drone hovered. While instrument drift was corrected reasonably well for $CO_2$ during the first 600 s, the last two profiles (with double correction frequency) showed considerably improved drift correction.

### 3.2 Examples using different flight patterns and tracer gas emission

#### 3.2.1 Box flights

In this example, a rewetted peatland was targeted using a box flight up to 30 m (Fig. 6). A $CO_2$ uptake can be seen from the forested eastern part (panel B), while the rewetted peatland itself is a net $CO_2$ sink, it is a source of $CH_4$ and $N_2O$ at the time

https://doi.org/10.5194/egusphere-2026-3826
Preprint. Discussion started: 17 August 2026


of measurements (Table 1). $CH_4$ concentration hotspots agree well with the streams and wettest areas being sources (panel A) given the wind directions at low altitudes. The $C_2H_6$ tracer-release, close to the upwind wall (marked in Fig. 6C) near a small waterfall, yielded a hotspot (panel C; northwest wall) at the same position as a $CH_4$ hotspot (panel A). There were trees growing with heights of 3-4 m in the upper left corner (backgrounds in Fig. 6) which could cause air close to the ground to be channeled along the edges of that area. See Fig. A1 for plots of in-flight instrument drift correction and Fig. A5 for interpolated wind speeds perpendicular to the walls.

The tracer makes it possible to conclude that the waterfall and the wettest areas contribute to the peaks in $CH_4$ concentration along the outgoing walls and that the wet areas, except the waterfall, seem to be associated with lower outgoing $CO_2$ concentrations closest to ground than the drier areas within the target area. Note that the concentrations shown here are not equivalent to fluxes and that fluxes require consideration of wind speed patterns along the walls.

https://doi.org/10.5194/egusphere-2026-3826
Preprint. Discussion started: 17 August 2026


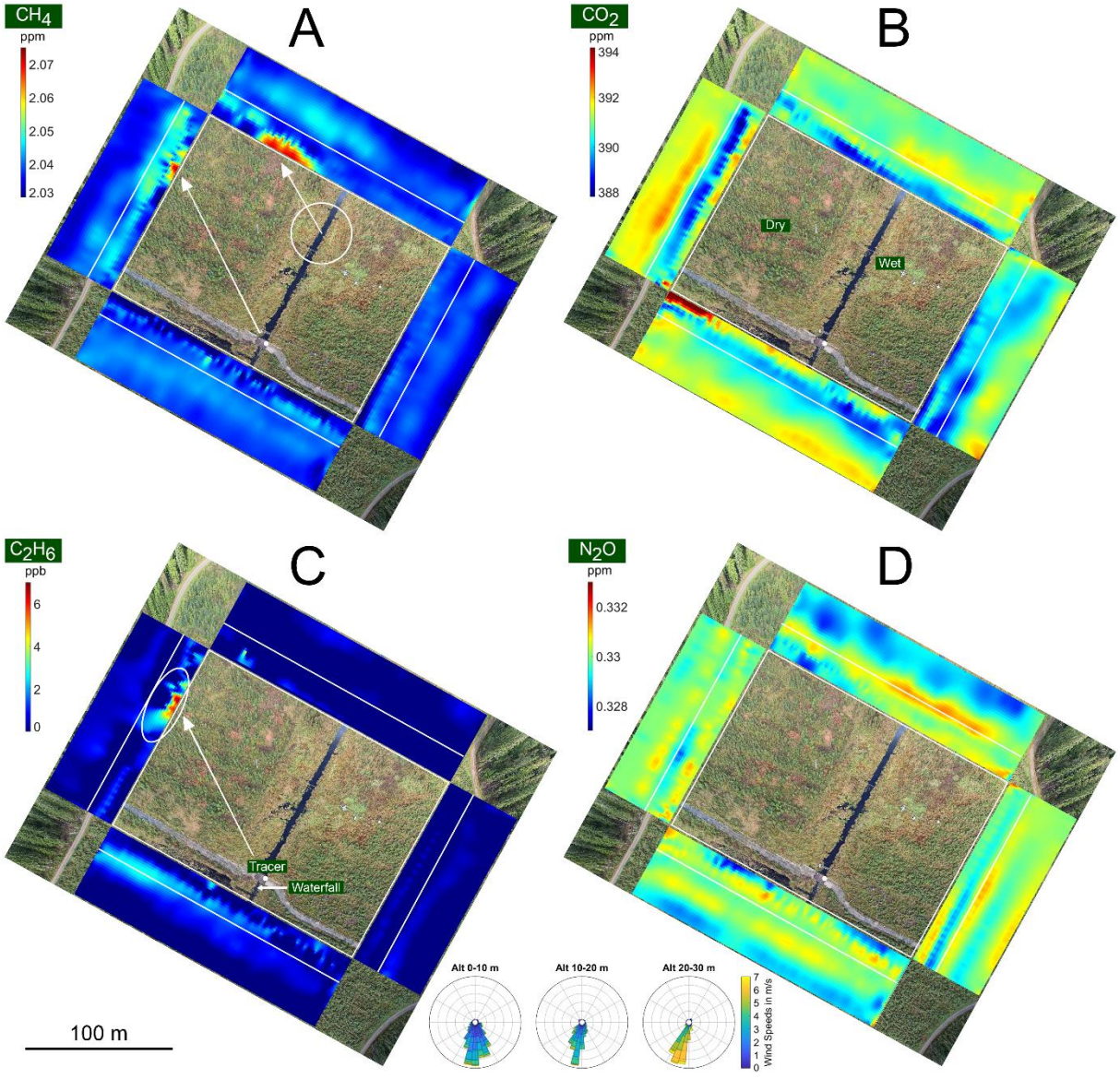


**Figure 6.** Box flight containing an area with rewetted peatland (2025-09-16, 11:05-11:30) using flight walls up to 30 m, tilted outwards in the panels for visual clarity. The release spot was chosen to be upwind of the area of interest (incoming air). Wall concentrations for the different gases are shown by the color scales in each panel (A-D) representing $CH_4$, $CO_2$, $C_2H_6$ (tracer), and $N_2O$, respectively. The white lines on the walls show the upper altitude included in the mass balance calculations (8 m). The box has a size of 151 x 122 meters. The background image is an overview shot taken with a separate camera drone in connection with the GHG measurements. A distribution of wind speed and wind direction for three different altitudes ranges are shown by the wind roses at the bottom.

https://doi.org/10.5194/egusphere-2026-3826
Preprint. Discussion started: 17 August 2026


The altitude profiles for this flight (see Figs. A7-A8 for $CH_4$ and $CO_2$, respectively) show increasing wind speed with altitude, especially above the treetops (about 20 m), a peak of $CH_4$ and $C_2H_6$ net flux (the latter released as a tracer gas) below 8 m and close to zero net flux above this altitude, a negative $CO_2$ net flux (uptake) below 5 m and a positive net flux above this altitude. Guided by these profiles, fluxes from the area of interest between the walls were calculated from the ground up to 8 m altitude (Table 1).

### 3.2.2 Two-wall flights

The two-wall approach can be advantageous as it allows measuring more altitudes (or repeated measurements) than box flights in the same amount of time. The assumption made is that most air of interest will pass through both walls due to the geometry. An example is shown in Figs. 7 and 8 where we did two flights (one for each wall) including many altitudes up to 100 meters to measure GHG fluxes from the littoral zone of a lake. A $C_2H_6$ tracer (2.8 liters per minute) was placed close to the vegetation of interest to mark its position on the outgoing wall (40 meters from the tracer) and the distance between the two walls were 181 meters. Emissions from both the tracer ($C_2H_6$) and littoral zone ($CH_4$) are seen as areas of higher concentration in the outgoing wall mainly below 10 m altitude, this shows that air at much higher altitudes (e.g. elevated $CO_2$ levels at 100 m (Fig. 8) are from much further distances with no connection to emissions in the area of interest). See Fig. A2 for plots of in-flight instrument drift correction, and Fig. A6 for a comparison of point clouds and Kriging-interpolated walls ($C_2H_6$ concentrations and perpendicular wind speed).

https://doi.org/10.5194/egusphere-2026-3826
Preprint. Discussion started: 17 August 2026


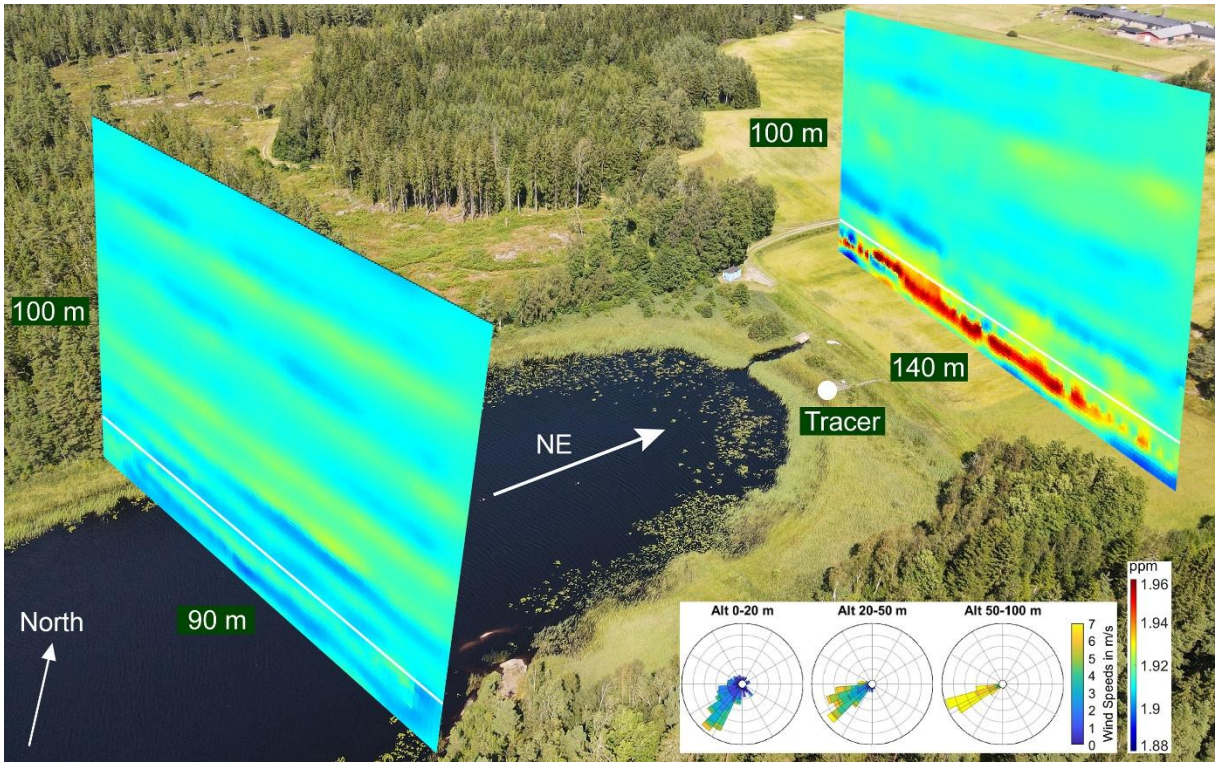


**Figure 7.** Two-wall flight focusing on the littoral zone of a lake with an incoming and an outgoing virtual wall up to 100 m perpendicular to the average wind direction (2024-07-23, 10:18-11:27). At low altitudes (up to 20-25 m, which is the height of the surrounding trees) the average wind direction was towards northeast which is along the extension of this narrow lake. A distribution of wind speeds and wind directions for different altitudes are shown by the wind roses at the bottom. The walls show $CH_4$ concentrations according to the color scale in the lower right. The white lines on the walls show the upper altitude included in the mass balance calculations (10 m).

https://doi.org/10.5194/egusphere-2026-3826
Preprint. Discussion started: 17 August 2026


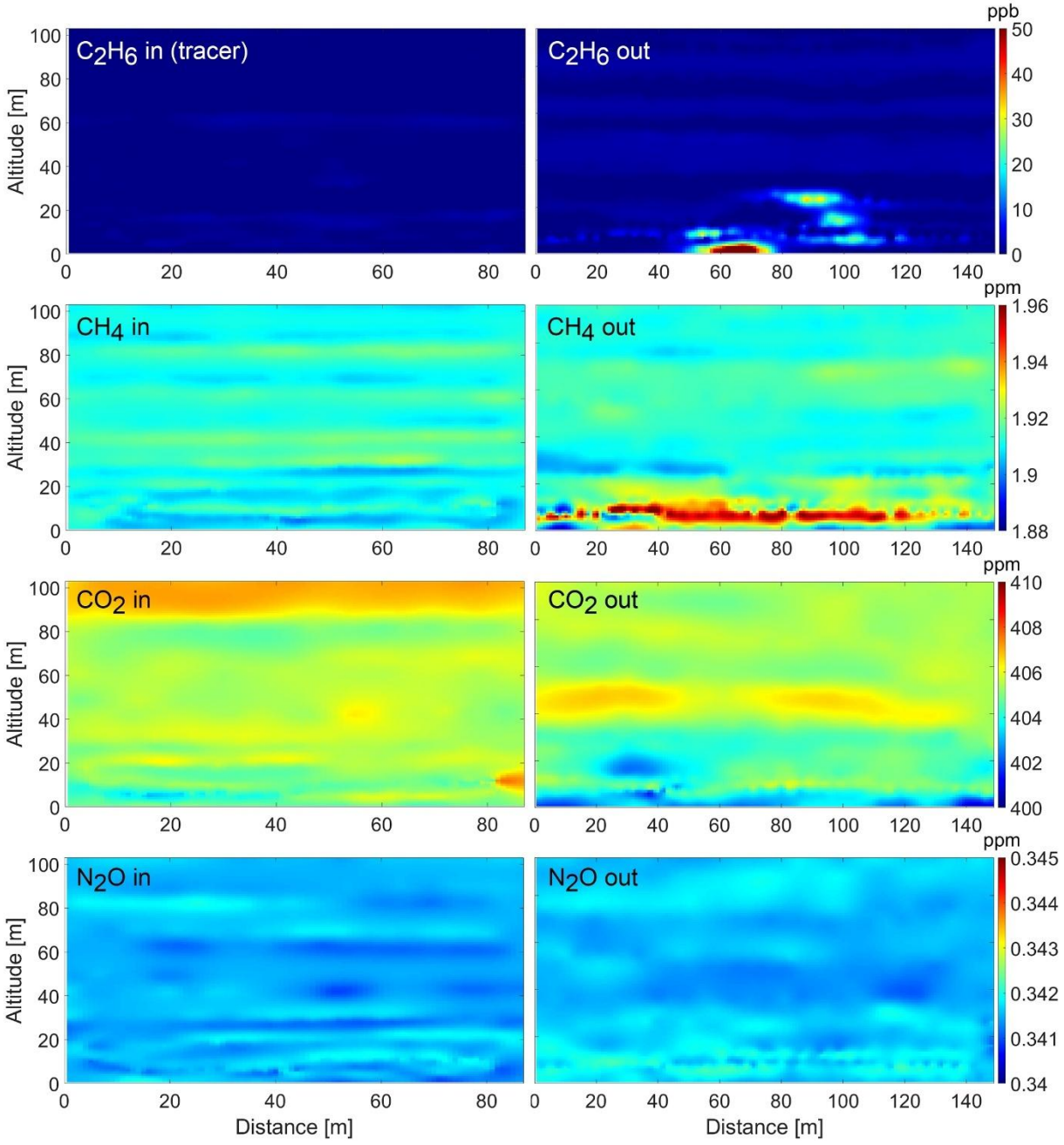


**Figure 8.** Concentrations of all the measured GHGs across the incoming and outgoing walls in the two-wall example (Fig. 7). The tracer ($C_2H_6$) is clearly seen with the main plume below 10 m altitude and smaller plumes reaching up to 15 m. This correlated well with the altitude of the much more extended $CH_4$ band from the reed vegetation in the littoral zone. A band of $CO_2$ uptake can be seen close to the ground in the outgoing wall probably from uptake by the littoral zone and grass on land,

https://doi.org/10.5194/egusphere-2026-3826
Preprint. Discussion started: 17 August 2026


with higher concentrations at higher elevations probably representing open water (higher altitudes). A very slight increase in $N_2O$-levels (about 1 ppb) can also be seen in the lower part of the outgoing wall that represents the littoral zone.

The altitude profiles for this flight (see Figs. A9-A10 for $CH_4$ and $CO_2$, respectively) clearly show increasing wind speed with altitude, a clear peak for both $CH_4$ and $C_2H_6$ net flux below 10 m, with some slightly elevated levels up to 20 m and close to zero net flux above this altitude. A negative $CO_2$ net flux (uptake) can be seen below 6 m and around zero net flux above this altitude (with fairly large variations at high altitudes; not related to the target area). Guided by these profiles, fluxes were calculated from the ground up to 10 m altitude (Table 1).

### 3.2.3 Long-wall flights

The simultaneous sampling of $CH_4$, $N_2O$, and $CO_2$ – together with $C_2H_6$ as a tracer, for cows in a barn and nearby open fertilizer tanks (Fig. 9), shows plume structures that are almost identical ($CH_4$ and $CO_2$) even though different instruments are used, indicating that they are well synchronized and that low emission levels can be accurately mapped with the system. The plume of $C_2H_6$ in the wall flight indicates the location in the point cloud corresponding to a gas flask placed mid-way between the open tanks and the barn, aiding in source separation. This shows the height reached by gas released at a given distance and helps separation of sources along the wall. The $C_2H_6$ tracer was placed upwind of the wall at a distance of 35 meters (3 liters per minute). See Fig. A3 for plots of in-flight instrument drift correction. Fluxes and uncertainties were calculated as illustrated in Fig. 3B, with areas not containing any plumes (Fig. 9) considered to be the background concentration (Table 1).

https://doi.org/10.5194/egusphere-2026-3826
Preprint. Discussion started: 17 August 2026


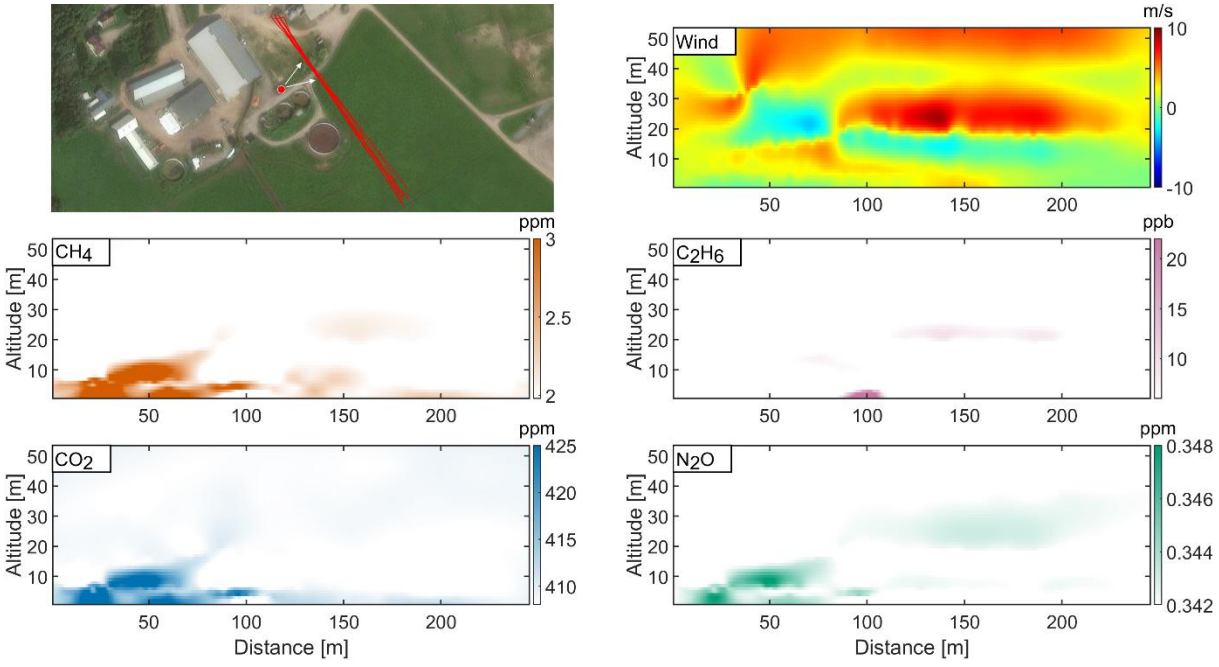


**Figure 9.** Long-wall flight outside of a barn with cows and open tanks (2024-08-19, 15:17-15:38). The tracer gas ($C_2H_6$) release position is marked with a red circle and two arrows showing variation in wind direction. The release spot was chosen to mark an area on the wall separating possible emissions from the open tanks (right) and the barn (left). The flight path is drawn with red lines (upper left panel). Gas concentration and wind maps are shown in the other panels. Emissions from the barn can be seen for all gases $CH_4$, $N_2O$, and $CO_2$ at a ground distance of 50 m (ventilation) and close to the ground at 50-100 m (open barn at the southern end), while $CH_4$ and $CO_2$ emissions are also seen from two smaller tanks at 120-150 m and a large tank at 200 m, close to the ground.

### 3.2.4 Low-altitude 2D-mapping flight

We demonstrate mapping of near-ground GHG accumulation under stable atmospheric conditions using horizontal mapping of $CH_4$, $N_2O$, and $CO_2$ over an area where a previously drained peatland had been rewetted (Fig. 10). During low-wind conditions, concentrations build up as hotspots above emissions sources and are not significantly dispersed horizontally. Under these conditions, it is possible to produce high-resolution maps in the environment at a low constant altitude to highlight hotspots and sinks of the different GHGs. The mapping was conducted in the early morning following the development of a stable nocturnal boundary layer during the night. See Fig. A4 for plots showing in-flight instrument drift correction. The northern part of the area was rewetted three years ago, while the southern part serves as a reference area that remains drained.

https://doi.org/10.5194/egusphere-2026-3826
Preprint. Discussion started: 17 August 2026


In this example we see a clear spatial difference between the different GHGs. $CH_4$ hotspots are seen over the central ditch and wettest areas in the northern part (some of which have open water and are likely bubbling). Water entering into the area from the north could have elevated gas concentrations as it comes from lake Följesjön which is a lake with extensive vegetation cover and a thick layer of organic matter rich sediment. Elevated $CH_4$ levels are also seen over water-filled old peat pits in the reference area. Higher $CO_2$ levels were clearly found more on the eastern side, both in the reference and rewetted areas, which could be due to moist air containing $CO_2$ coming down from the forest slope during night. The southernmost $CO_2$ peak was near a stream waterfall at the forest edge. The $N_2O$ differences were small (< 1 ppb) with a more complex pattern than for $CH_4$ and $CO_2$. One of the locations with highest $N_2O$ concentration coincides with a location of high $CO_2$ near the forest edge waterfall (lower right). No tracer gas was used in this test. Such 2D-mapping flights in low-wind conditions illustrate how the iUAS-$F_{GHG}$ approach can be used to map areas that are otherwise inaccessible. One such application could be mapping of gas leaks (Wietzel and Schmidt, 2023) where there are no roads available.

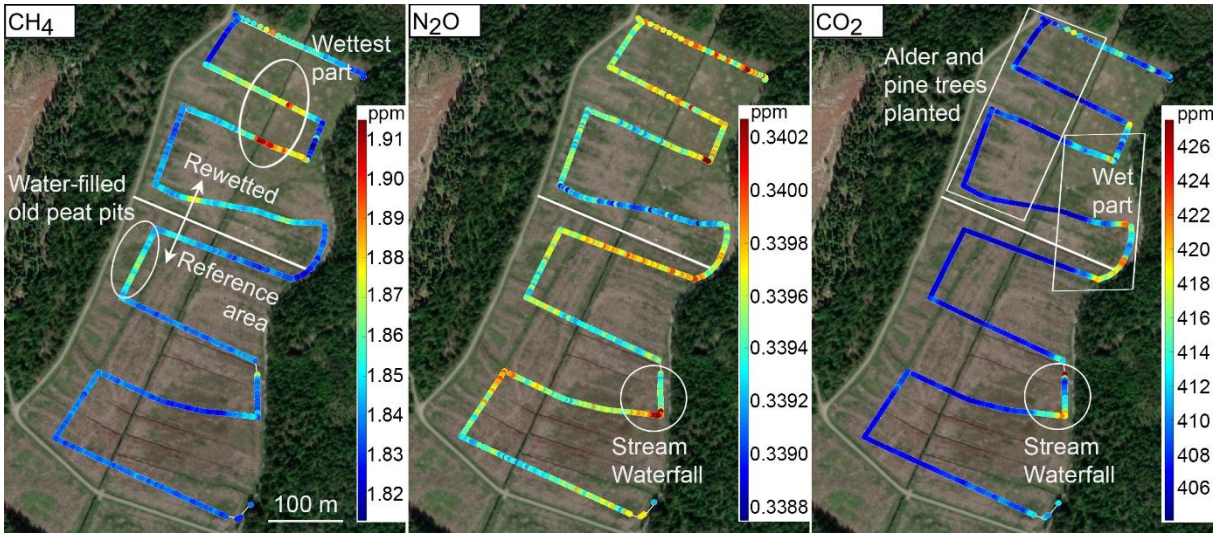


**Figure 10.** 2D-maps of $CH_4$, $N_2O$, and $CO_2$ in a partially rewetted peatland (2024-09-02, 18:46-19:10) after instrument drift correction (see Fig. A4). The area shown in each panel has a size of 500 x 700 m and flight paths were flown at an altitude of about 3 meters during very calm wind conditions. The thick white line marks the division between the rewetted (north) and reference area (south).

### 3.2.5 Flux measurements

Results from the different flight patterns and environments used as examples in this method study are presented in Table 1. The tracer could be detected in all environments where it was used. For the box flight the tracer was not used quantitatively, it was instead only used as a tracer of air movement. In the other cases $C_2H_6$ fluxes agreed well with the corresponding

https://doi.org/10.5194/egusphere-2026-3826
Preprint. Discussion started: 17 August 2026


known release rates (see method section). For all the environments, the vertical extent of the tracer gas on the downwind flight walls provided information about the altitude below which air was influenced by exchange with the area of interest.

**Table 1.** Emissions from the environments in this study (mean ± 1 SD). For the two-wall and box flights the enclosed ground area is given in the notes-column.

| Environment | Flight pattern | $CH_4$ flux $mg \cdot s^{-1}$ ($mg \cdot m^{-2} \cdot d^{-1}$) | $N_2O$ flux $mg \cdot s^{-1}$ ($mg \cdot m^{-2} \cdot d^{-1}$) | $CO_2$ flux $mg \cdot s^{-1}$ ($mg \cdot m^{-2} \cdot d^{-1}$) | $C_2H_6$ flux $mg \cdot s^{-1}$ ($ml \cdot s^{-1}$) | $C_2H_6$ tracer release ($ml \cdot s^{-1}$) | Notes |
|---|---|---|---|---|---|---|---|
| Rewetted peatland | Box flight | 15.7 ± 3.8 (74 ± 18) | 0.3 ± 0.9 (1.2 ± 4.3) | -1 470 ± 1 180 (-6 900 ± 5 600) | * * | | 18 350 $m^2$ (151 x 122 m) |
| Lake littoral zone | Two walls | 70.3 ± 6.2 (207 ± 19) | 2.9 ± 1.2 (8.6 ± 3.5) | -2 700 ± 1 900 (-7 900 ± 5 800) | 69 ± 15 (54 ± 12) | (46 ± 2.2) | 29 350 $m^2$ (181 x 162 m) |
| Open tanks | Long wall | 165 ± 16 | --- | 2810 ± 80 | 68 ± 0.8 (53 ± 0.6) | (50 ± 2.4) | Wall 35 m downwind of the tracer source. |
| Barn with cows | Long wall | 264 ± 4.4 | 8.5 ± 1.4 | 3 651 ± 295 | 68 ± 0.8 (53 ± 0.6) | (50 ± 2.4) | Wall 35 m downwind of the tracer source. |

* Tracer gas was only used to track air motion

The measured $CH_4$ and $CO_2$ emissions in the rewetted peatland and at the lake littoral zone are comparable with relevant literature reviews (Table A1)(Bianchi et al., 2021; Cao et al., 2024; Kasimir Klemedtsson et al., 2024; Milberg et al., 2017). Many reviews prioritize reporting whole-year integrated fluxes, while our observed fluxes represent daytime fluxes at peak growth season. Such fluxes could be extracted for $CH_4$ and $CO_2$ from a previous flux chamber study at the same lake littoral zone as studied here (Milberg et al. 2017) having corresponding flux rates as those of the present study (Table A1).

The $N_2O$ fluxes at the rewetted peatland and the lake littoral zone were higher in the present study than in the literature reviews used for comparison (Table A1). One reason could be the difference between integrated yearly values in the reviews versus daytime peak growth season in this study, and also that $N_2O$ fluxes can vary greatly in space and be substantially higher at locations recently being moist but drying up (Liengaard et al., 2013) - e.g. at embedded elevated surfaces in

https://doi.org/10.5194/egusphere-2026-3826
Preprint. Discussion started: 17 August 2026


wetlands that may not be prioritized as wetlands in flux chamber assessments but are covered by the integrated iUAS assessments.

Regarding the emission from the barn with cows, literature (Cottle et al., 2011) gives a reference emission of 67.5 - 98.6 kg $CH_4 \cdot yr^{-1} \cdot cow^{-1}$ depending on the type of cow and feed. For our measurements of a barn with 63 cows, this measurement corresponds to an emission of 132.2 ± 2.2 kg $CH_4 \cdot yr^{-1} \cdot cow^{-1}$ which is above the upper limit of the reference emission; this is expected as manure inside the barn is also included in the total flux.

### 3.3 Method discussion

In recent years there has been fast evolution in methods using UASs to measure GHG emissions (Table 2). Two main techniques can be found: (i) using a onboard laser and detector to scan profiles or walls from a certain height – yielding column density measurements, and (ii) making a point cloud of concentrations with in-situ measurements at the UAS, such as the iUAS method used in this study, that also measures wind at the drone position. Both techniques have their different advantages and disadvantages.

Column density methods are time-efficient, as a drone can fly between two GPS coordinates at a fixed altitude and scan a wall. However, achieving high sensitivity may require a retroreflector, which can be difficult to deploy in many environments. These measurements do not provide wind speed data that are spatially compatible with the GHG concentration measurements, which generate uncertainties in the flux quantification. If column density is measured below the drone, it is possible that measurements are influenced by the rotor downwash. However, the column density approach can be highly beneficial when time-efficiency is more important than flux accuracies.

The iUAS approach used here has the advantage that all measurements needed for flux calculation are being synchronously made on the drone itself. This is advantageous for reducing spatiotemporal mismatch because wind transport and GHG concentrations can be linked. However, the influence of sensor drift needs to be considered. For high concentration levels with clear and quick spikes (short durations when the drone passes a plume), a baseline can be fitted and sensitivity to instrument drift is limited (Dooley et al. 2024). For lower concentrations, it has been suggested to let gas analyzers stabilize for hours before conducting profile flights (Bolek et al. 2024). We found in our case, that running the gas analyzers on an external battery for several hours before taking off does not stabilize the drift during flight, because increased drift was associated with take-off (due to temperature drift in the gas analyzers in flight). Drift correction by post-processing has proven far from trivial, and the ability to correct gas analyzer drift in-flight as presented here increases the sensitivity of iUAS-GHG mapping. This seems needed for current low-weight gas analyzers and sensors to reach the high precision needed for quantifying natural emissions and low anthropogenic emissions by drone. We found no prior studies in the literature using tracer gas emissions or in-air drift correction in combination with iUAS GHG measurements. In this study

https://doi.org/10.5194/egusphere-2026-3826
Preprint. Discussion started: 17 August 2026


we have shown that multiple GHGs can be measured and compared, with in-flight drift correction, and tracer gas emissions at strategic spots to match footprints for sources of interest to the corresponding UAS point cloud data.

A future potential for improved assessments of low emissions or extended sources with the iUAS method is repeated box flights with all walls being measured close in time. This reduces the uncertainty from changes in wind conditions between separate wall flights. With repeated flights and averaging, the drift correction may also be further improved as slight over- and underestimations in gas concentrations at the same altitude will likely partially cancel each other out. Gas sensors with less drift are obviously beneficial but at present come with greater weight, in practice reducing the number of gases that can be measured simultaneously on a given drone. Future light-weight optical gas analyzers that have less drift would improve the method, but until then high accuracy will depend on successful drift correction. We hope the iUAS-approaches presented here will facilitate sensitive, accurate, and widespread multi-GHG flux measurements with presently available technology and reasonably sized drones, to provide guidance for effective emission mitigation as rapidly as possible.

**Table 2.** A summary of the recent evolution in methods for GHG measurements using UASs.

| Source | Environment | Method | Notes |
|---|---|---|---|
| Gålfalk et al. 2021 | $CH_4$ emissions from wastewater treatment | UAS with gas, wind, telemetry, and meteorological sensors onboard the drone. | Flux uncertainty of 94 mg·$CH_4$·$s^{-1}$ for a source emitting 20 600 mg $CH_4$·$s^{-1}$ |
| Corbett and Smith 2022 | $CH_4$ emissions from oil and gas production assets and other industrial emissions. | Miniature tunable diode laser absorption spectroscopy (TDLAS) instrument on a UAS. Separate wind measurements at 1.5 m above ground (not on UAS). | Emission rates of 280–7000 kg·$h^{-1}$ for point sources studied. Error estimates versus flight patterns up to 36% (i.e. > ±100 mg $CH_4$·$s^{-1}$). |
| Liu et al. 2022 | $CO_2$ using low-weight sensor | UAS with a low-cost nondispersive IR $CO_2$ sensor. | Accuracy 2 ppm at 1 Hz |
| Olaguer et al. 2022 | Landfill $CH_4$ emissions | TDLAS for $CH_4$ mounted on UAS. Wind profile from separate UAS at fewer locations. | |
| Scheller, Mastepanov, and Christensen 2022 | High-arctic fen | UAS with tube to ground-based analyzer. Separate wind measurements (not on UAS). | |

https://doi.org/10.5194/egusphere-2026-3826
Preprint. Discussion started: 17 August 2026


| | | | |
|---|---|---|---|
| Wilson et al. 2022 | UAS wind data, any env. | Anemometer measurements through different placements. | |
| Cossel et al. 2023 | Controlled releases of $CH_4$ and $C_2H_6$ | UAS-assisted laser spectroscopy (dual-comb spectrometer). UAS-mounted retroreflector. Separate wind measurements (not on UAS). | Flux detection limit 0.03 g $CH_4 \cdot s^{-1}$. 23 ppm·m sensitivity in 16 s measurement time over pathlengths of 200 m. |
| De Souza Maria et al. 2023 | $XCH_4$ from fires in The Amazon | Remote sensing | UAS mentioned as future alternative |
| Filkin, Lipin, and Sliusar 2023 | $CH_4$ leaks in landfills and municipal solid waste | 2D-mapping of column concentrations under the UAS to find leaks (hotspot map) | No wind measurements on UAS and no fluxes |
| Hashim et al. 2023 | Mapping GHGs and air pollutants over industrial area. | Sniffer4D; 1 ppm/1 s; $CO_2$, $CH_4$, CO, $O_3$ + $NO_2$, and $SO_2$; on UAS. Unclear if wind measurements were made or generated from meteorological monitoring. | Fluxes not quantified. Focus on concentration maps. |
| Song et al. 2023 | $CH_4$ emissions from wastewater collection and treatment systems | Review | No original data or new methods. |
| Soskind et al. 2023 | $CH_4$ leak detection | UAS-assisted laser dispersion spectroscopy. UAS-mounted retroreflector. Separate wind measurements (not on UAS). | Flux detection limit 130 mg $CH_4 \cdot s^{-1}$ (2.3 ppm·m sensitivity over pathlengths of 40–150 m). |
| Wang et al. 2023 | Remote sensing of $CH_4$ | 2-tiered framework for measurements | Pointing at UAS as possible supplement to satellite measurements. |
| Bolek, Heimann, and Göckede 2024 | $CO_2$ and $CH_4$ flux from Subarctic | 2D-mapping at 10 m (hotspots) and vertical profiles. $CO_2$, $CH_4$, and anemometer on the UAS | Fluxes calculated from vertical profiles. |

https://doi.org/10.5194/egusphere-2026-3826
Preprint. Discussion started: 17 August 2026


| | | | |
|---|---|---|---|
| | permafrost peatland | | |
| Dimitriadou et al. 2024 | Wastewater treatment plants (WWTPs) | Theoretical | Fit-for-purpose UAS systems suggested for WWTPs |
| Dooley et al. 2024 | $CH_4$ and $C_2H_6$ from point sources and landfills | Repeated plume transects at different altitudes. UAS equipped with $CH_4$ + $C_2H_6$ gas instrument and anemometer. | |
| Han et al. 2024 | $CO_2$ and $CH_4$ from coking plant smoke stacks | Gas samples into a long tube. Box flight pattern. Cavity ring-down spectroscopy of sampled air after landing. Anemometer mounted on drone. | |
| Liu et al. 2024 | $CH_4$ in mountainous area | Vertical profiles from sampling into gas bags at discrete altitudes | No wind measurements on UAS and no fluxes |
| Tassielli, Cananà, and Spalatro 2024 | Controlled $CH_4$ releases | Miniature tunable diode laser absorption spectroscopy (TDLAS) instrument on UAS. Separate wind measurements by weather station (not on UAS). | Agriculture, suburban, and industrial areas considered to have "no emissions" |
| Yong et al. 2024 | $CH_4$ at landfills | Wall flights downwind of landfill. Anemometer on-board the UAS. | |
| Zhu et al. 2024 | $CO_2$ and $CH_4$ from dairy farm | Gas samples into a long tube. Vertical profiles in suspected hot spot areas. Spectroscopy of sampled air after landing. Wind calculated from tilt of UAS. | Flux calculated from dispersion model |
| Gålfalk and Bastviken 2025 | $CH_4$, $N_2O$, and $CO_2$ emissions from wastewater treatment | UAS with gas, wind, telemetry, and meteorological sensors onboard the drone. | Mean flux uncertainty 75 mg $CH_4 \cdot s^{-1}$ and 15 mg $N_2O \cdot s^{-1}$ |
| Kim et al. 2025 | $CO_2$ from municipal solid waste | Mass balance and inverse Gaussian methods. $CO_2$ sensor with a resolution of 1 ppm. Anemometer mounted on drone. | |

https://doi.org/10.5194/egusphere-2026-3826
Preprint. Discussion started: 17 August 2026


| | | | |
|---|---|---|---|
| | incineration | | |
| Moormann et al. 2025 | $CO_2$ in semi-urban environment | Vertical profiles of air quality including $CO_2$ | |
| Scheutz et al. 2025 | $CH_4$ at a biogas plant and controlled releases | Wall flights downwind of the biogas plant. Anemometer on-board the UAS. Simultaneous comparison with the tracer gas dispersion method, agreeing well with the UAS-based method. | Drone method uncertainty 1720 mg $CH_4 \cdot s^{-1}$ and tracer gas dispersion uncertainty 1220 mg $CH_4 \cdot s^{-1}$. Emission of about 7100 mg $CH_4 \cdot s^{-1}$. |
| Van Hove et al. 2025 | $CH_4$ emissions from African livestock | UAS and Bayesian inference method | Detection limit of 28 mg $CH_4 \cdot s^{-1}$ and uncertainty of 14 mg $CH_4 \cdot s^{-1}$ |

https://doi.org/10.5194/egusphere-2026-3826
Preprint. Discussion started: 17 August 2026


## Appendix A

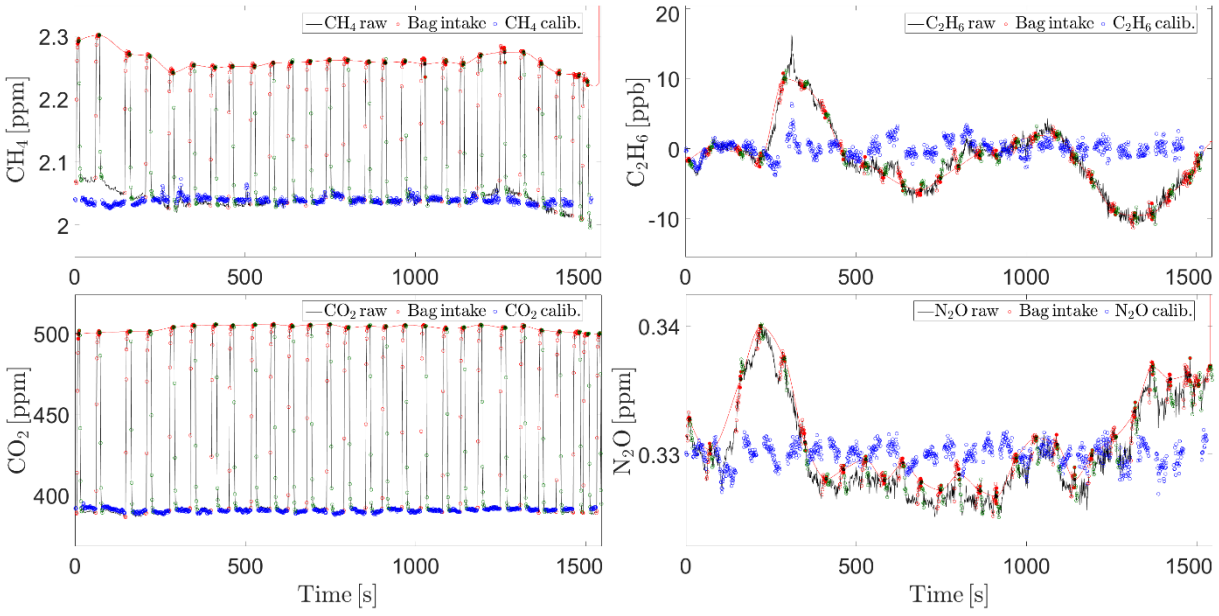


**Figure A1.** Sensor raw data drift and correction for the box flight over a rewetted peatland (Fig. 6). Data shown are raw (black) and calibrated (blue) concentrations of simultaneously sampled $CH_4$, $C_2H_6$ (tracer gas), $CO_2$, and $N_2O$, respectively. Red symbols and fitted curves indicate drift calibration points when air was measured from the on-board gas bag.

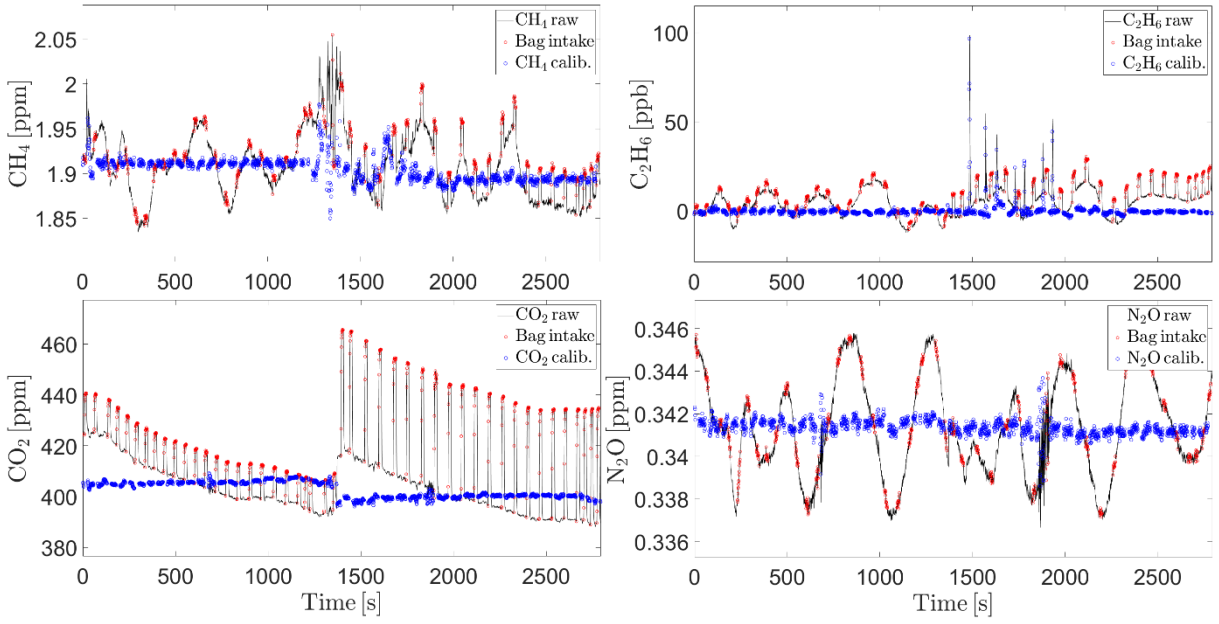

https://doi.org/10.5194/egusphere-2026-3826
Preprint. Discussion started: 17 August 2026


**Figure A2.** Sensor raw data and drift correction for the two-wall flights at the littoral zone of a lake (Fig. 8). Data shown are raw (black) and calibrated (blue) concentrations of simultaneously sampled $CH_4$, $C_2H_6$ (tracer gas), $CO_2$, and $N_2O$, respectively. Red symbols and fitted curves indicate drift calibration points when air was measured from the on-board gas bag. The fast variation in gas concentrations at ~1300 s ($CH_4$) and ~1850 s ($N_2O$) was caused by bad spectral fits by the gas analyzers (these points are not used in the flux calculations). These plots were made from two flights (0-1350 s for the incoming and 1350-2700 s for the outgoing wall) which shows a shift in gas concentrations after relative drift correction. For the flux calculation the absolute levels are intercalibrated for the two flights using the assumption of constant concentrations at high altitude during the flights.

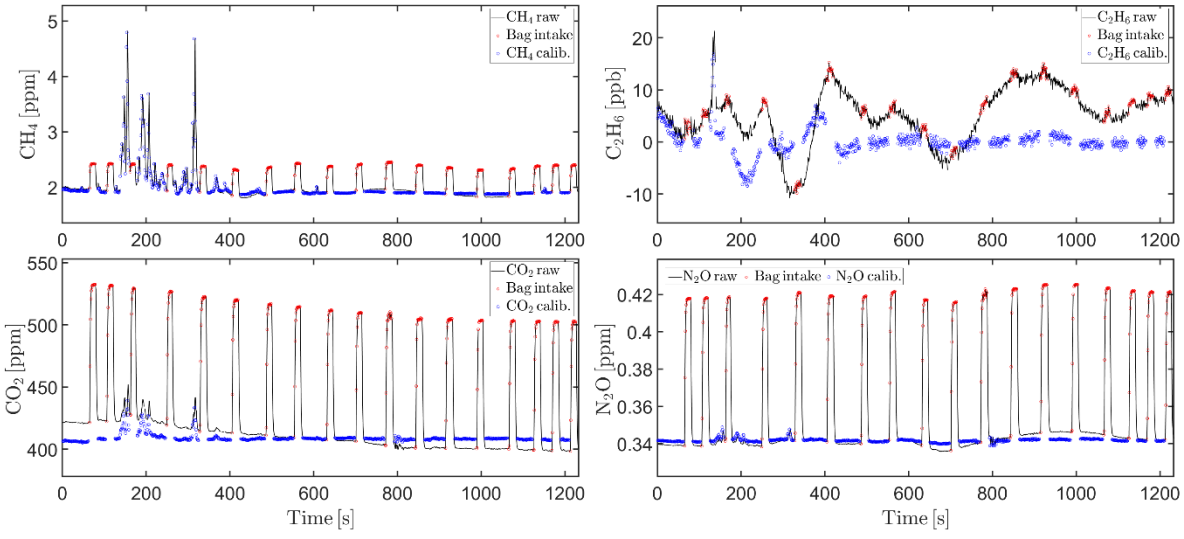


**Figure A3.** Sensor raw data and drift correction for the wall flight outside a barn with cows and open tanks (Fig. 9). Data shown are raw (black) and calibrated (blue) concentrations of simultaneously sampled $CH_4$, $C_2H_6$ (tracer gas), $CO_2$, and $N_2O$, respectively. Red symbols and fitted curves indicate drift calibration points when air was measured from the on-board gas bag. (In the $C_2H_6$ panel, the dip to -10 ppb at ~200 s in the calibrated curve, which is unrealistic, is illustrative and shows how drift calibration fails if references data is sampled too infrequent relative to the drift variations, in this case missing a "drift dip").

https://doi.org/10.5194/egusphere-2026-3826
Preprint. Discussion started: 17 August 2026


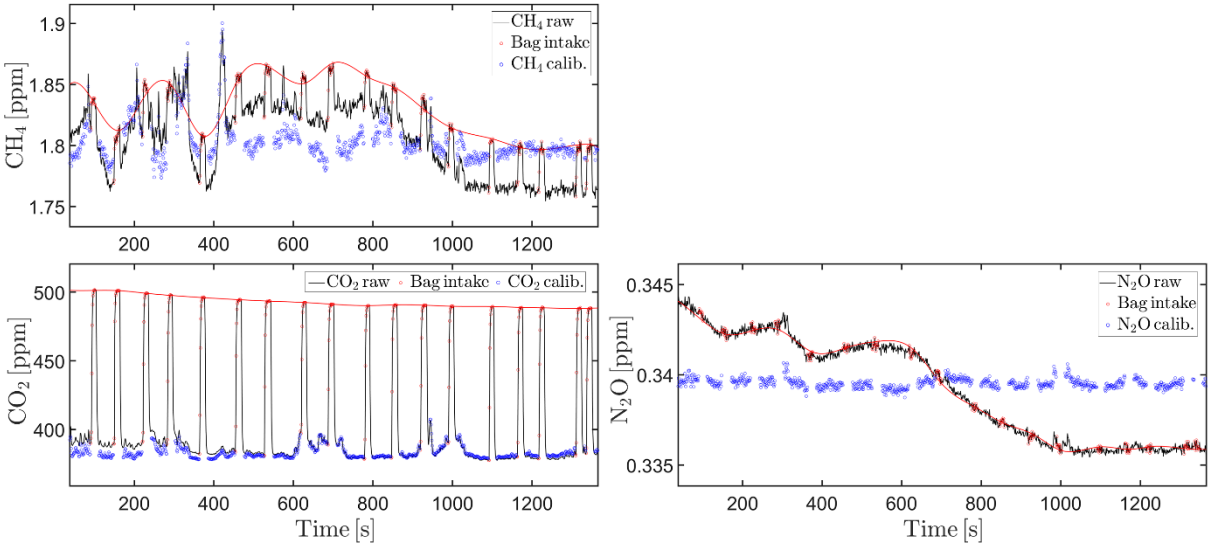


**Figure A4.** Sensor raw data and drift correction for the 2D-mapping at low altitude over a rewetted wetland area (Fig. 10). Data shown are raw (black) and calibrated (blue) concentrations of simultaneously sampled $CH_4$, $CO_2$, and $N_2O$, respectively. Red symbols and fitted curves indicate drift calibration points when air was measured from the on-board gas bag.

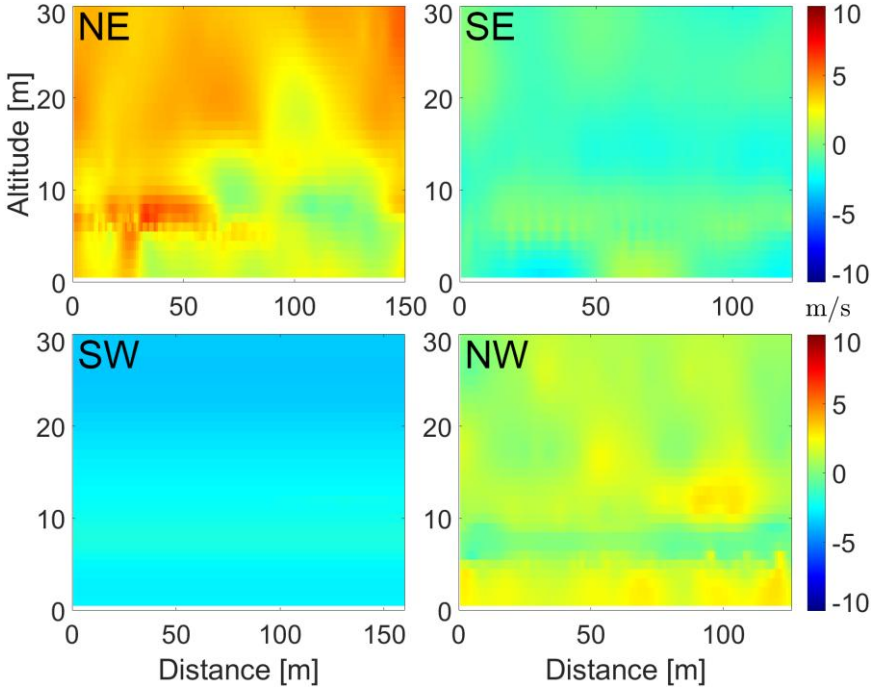

https://doi.org/10.5194/egusphere-2026-3826
Preprint. Discussion started: 17 August 2026


**Figure A5.** Interpolated wind speeds perpendicular to the virtual walls of the rewetted peatland case (Fig. 6). Each wall (panel) is labelled with its cardinal direction relative to the center of the boxed area. The wind speeds are defined as positive or negative if they are directed out of or into the boxed area, respectively.

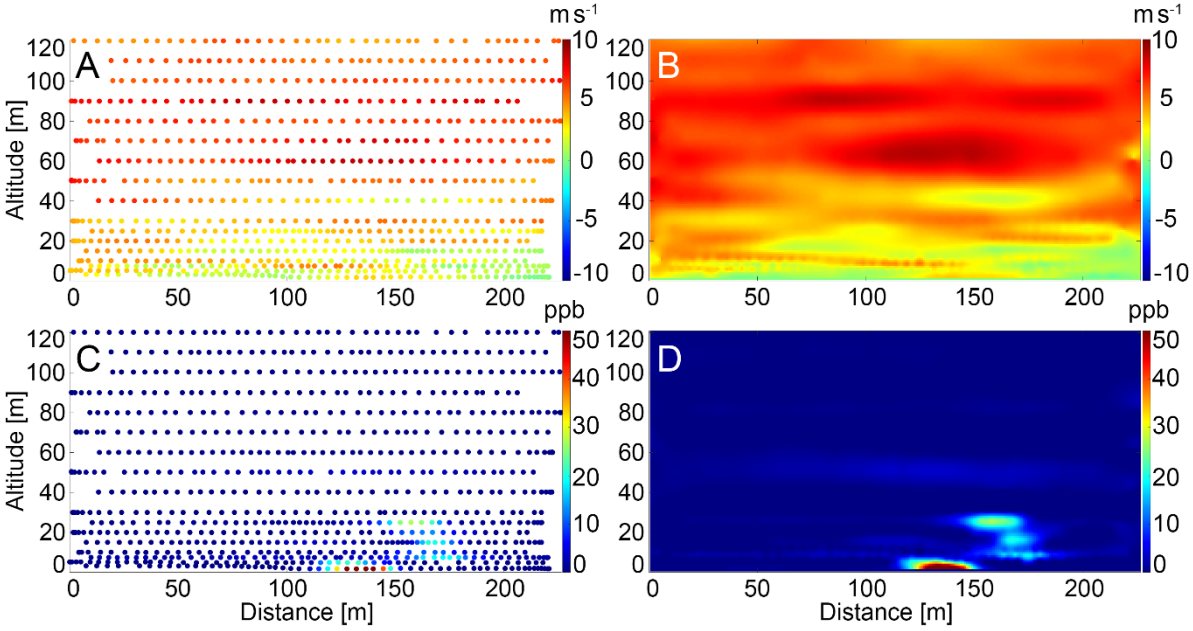


**Figure A6.** Example displaying measured (panels A, C) and interpolated (panels B, D) perpendicular wind speeds and $C_2H_6$ concentrations, respectively, for a virtual wall downwind of the lake with a tracer (Fig. 8).

https://doi.org/10.5194/egusphere-2026-3826
Preprint. Discussion started: 17 August 2026


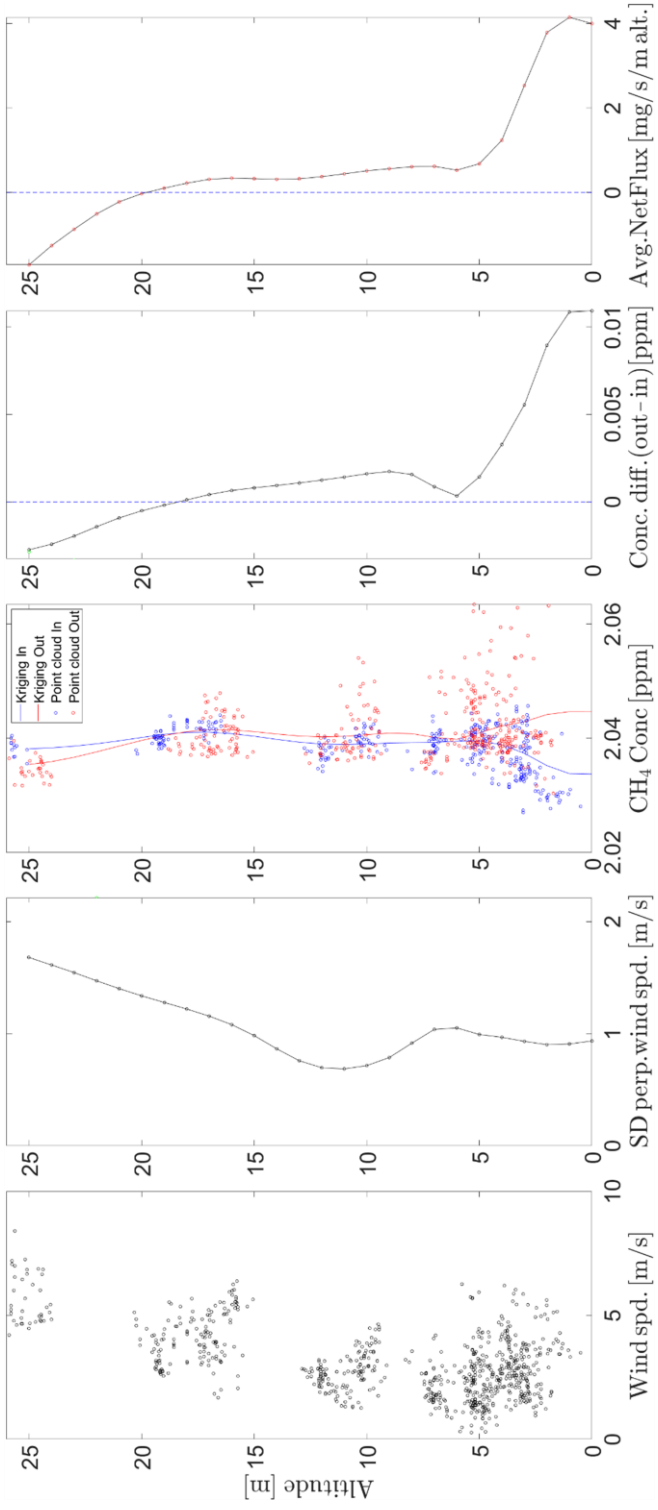


**Figure A7.** Wind, $CH_4$ and net Flux profiles for the box case (Fig. 6). The panels are (from left to right): wind speed (point cloud), standard deviation of wind speeds perpendicular to walls, $CH_4$ concentration, concentration difference between outgoing and ingoing walls, and the average net flux (from Kriging interpolated wall data). To reflect the contribution of each wall to the flux in these plots, the concentration difference profiles (conc. diff. out-in) and the standard deviations of wind speeds perpendicular to walls (SD perp. wind spd.) were weighted by the average perpendicular wind speed for each wall at each altitude interval.

https://doi.org/10.5194/egusphere-2026-3826
Preprint. Discussion started: 17 August 2026


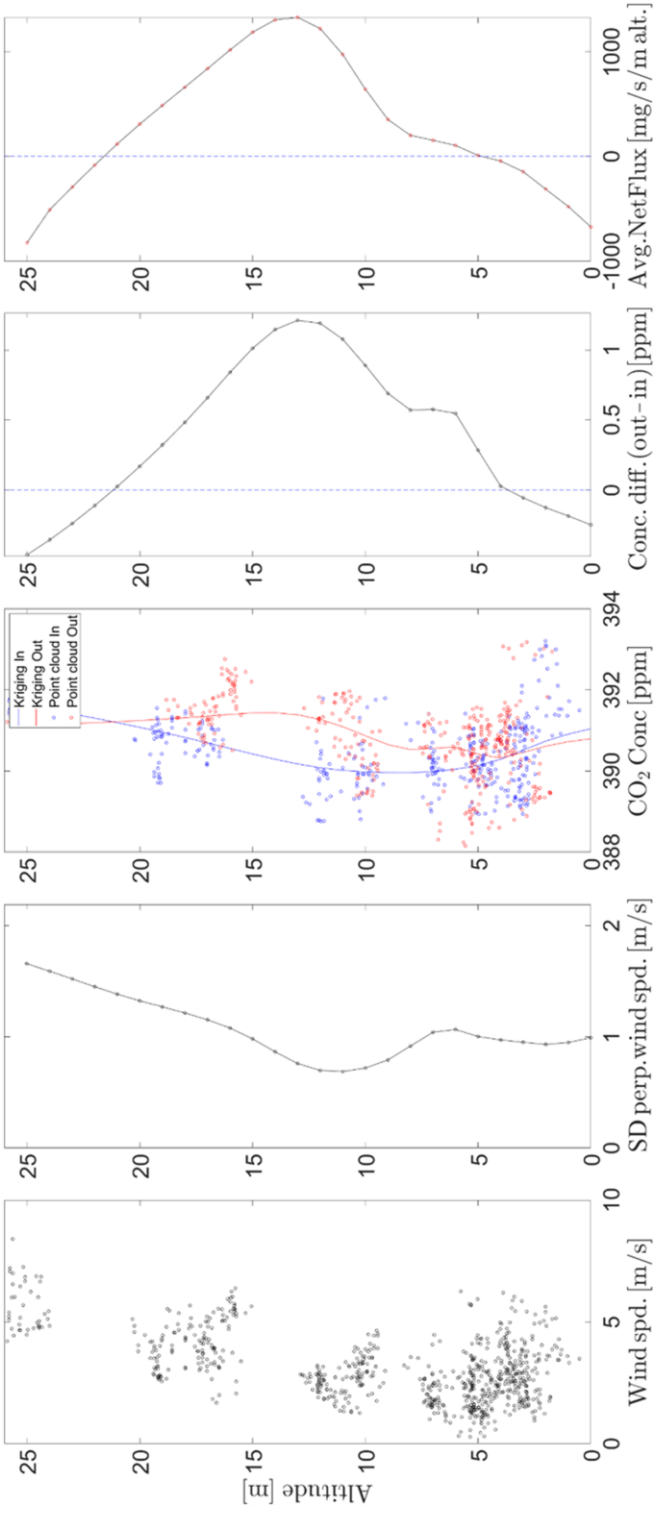


**Figure A8.** Wind, CO2 and net Flux profiles for the box case (Fig. 6). The panels are (from left to right): wind speed (point cloud), standard deviation of wind speeds perpendicular to walls, CH4 concentration, concentration difference between outgoing and ingoing walls, and the average net flux (from Kriging interpolated wall data). To reflect the contribution of each wall to the flux in these plots, the concentration difference profiles (conc. diff. out-in) and the standard deviations of wind speeds perpendicular to walls (SD perp. wind spd.) were weighted by the average perpendicular wind speed for each wall at each altitude interval.

https://doi.org/10.5194/egusphere-2026-3826
Preprint. Discussion started: 17 August 2026


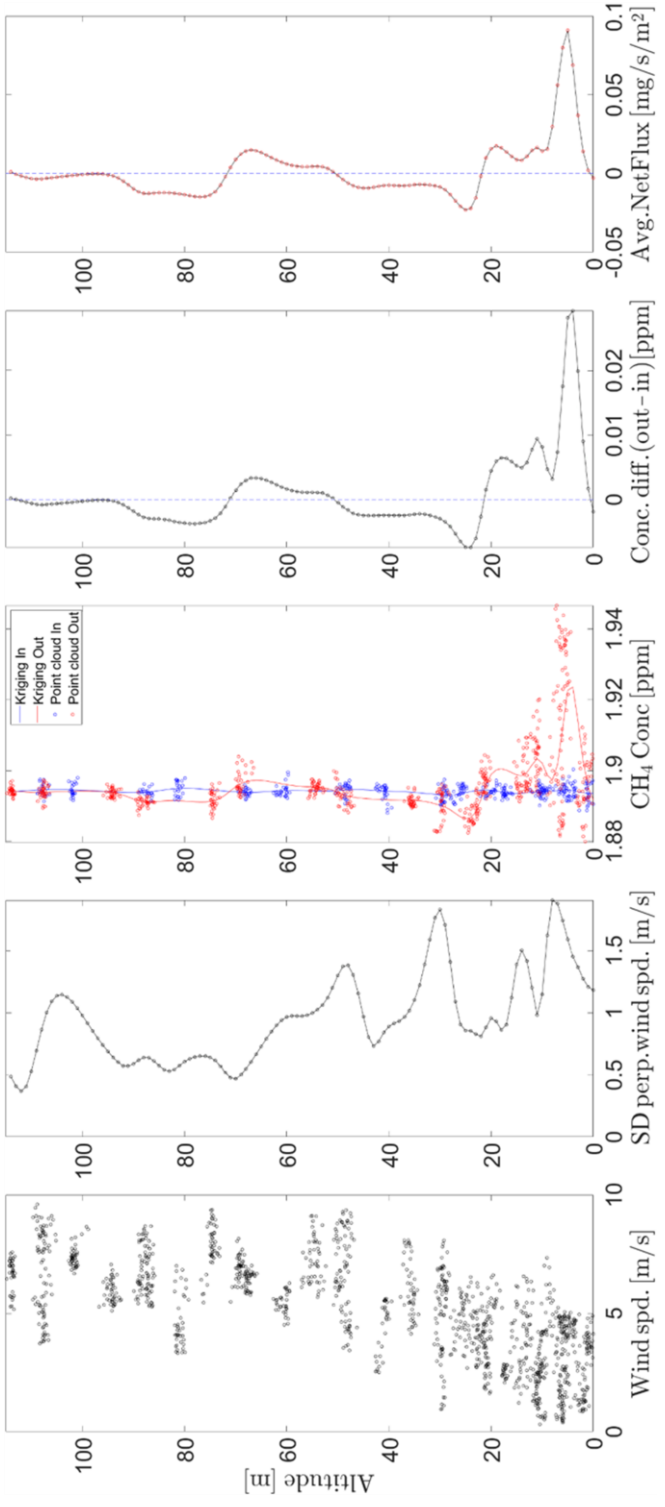


**Figure A9.** Wind, $CH_4$ and net Flux profiles for the two-wall case (Fig. 8). The panels are (from left to right): wind speed (point cloud), standard deviation of wind speeds perpendicular to walls, $CH_4$ concentration, concentration difference between outgoing and ingoing walls, and the average net flux (from Kriging interpolated wall data). To reflect the contribution of each wall to the flux in these plots, the concentration difference profiles (conc. diff. out-in) and the standard deviations of wind speeds perpendicular to walls (SD perp. wind spd.) were weighted by the average perpendicular wind speed for each wall at each altitude interval.

https://doi.org/10.5194/egusphere-2026-3826
Preprint. Discussion started: 17 August 2026


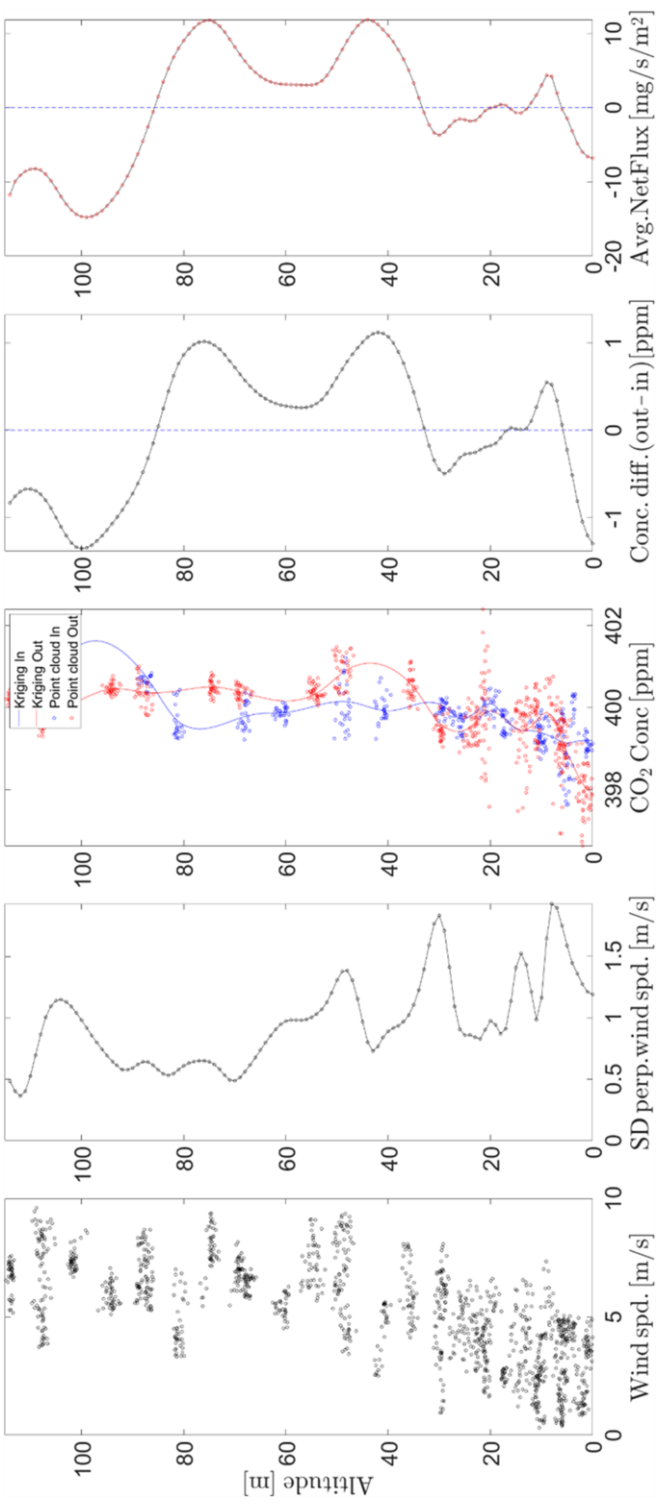


**Figure A10.** Wind, $CO_2$ and net Flux profiles for the two-wall case (Fig. 8). The panels are (from left to right): wind speed (point cloud), standard deviation of wind speeds perpendicular to walls, $CH_4$ concentration, concentration difference between outgoing and ingoing walls, and the average net flux (from Kriging interpolated wall data). To reflect the contribution of each wall to the flux in these plots, the concentration difference profiles (conc. diff. out-in) and the standard deviations of wind speeds perpendicular to walls (SD perp. wind spd.) were weighted by the average perpendicular wind speed for each wall at each altitude interval.

**Table A1**. Flux comparisons with literature reviews on GHG fluxes from rewetted or natural wetlands in boreal or temperate and nitrogen rich settings.

| Source | Context | Format | $CH_4$ mg $m^{-2}$ $d^{-1}$ | $N_2O$ mg $m^{-2}$ $d^{-1}$ | $CO_2$ mg $m^{-2}$ $d^{-1}$ | Notes |
|---|---|---|---|---|---|---|
| Bianchi et al 2021 | Wetland restoration former agricultural soil | mean (min and max) | 41 (24-58) | 0.50 (0.05 - 1.00) | -959 (-1634 to -384) | Whole year values. |
| Cao et al 2024 | Marsh wetlands China | mean ± 1SD | 71 ± 108 | 0.624 ± 0.67 | 634 ± 6003 | Whole year values. |
| Kasimir & Lindgren 2024 | Boreal mire | mean (low and high CI) | 19 (14 - 27) | 0.032 (0.019 - 0.066) | -513 (-671 to -236) | Whole year values. Review from Annex 1 |
| Kasimir & Lindgren 2024 | Boreal flooding | mean (low and high CI) | 62 (52 - 74) | 0.11 (0.05 - 0.25) | -372 (-477 to -241) | Whole year values. Review from Annex 1 |
| Kasimir & Lindgren 2024 | Temperate bog end fen | mean (low and high CI) | 24 (16 - 33) | 0.077 (-0.025 to 0.252) | -375 (-614 to -77) | Whole year values. Review from Annex 1 |
| Kasimir & Lindgren 2024 | Temperate flooding other vegetation | mean (low and high CI) | 129 (90 - 178) | 0.14 (0.02 - 0.26) | -60 (-340 to 258) | Whole year values. Review from Annex 1 |
| Kasimir & Lindgren 2024 | Flooding of Phragmites | mean (low and high CI) | 171 (137 - 192) | nd | nd | Whole year values. Review from Annex 1 |
| Milberg et al 2017 | Chamber measurements light period in July at Erssjön littoral zone | mean (min and max) | 214 (95 - 602) | nd | -16940 (-59365 to -4048) | Peak growth season. Daytime. |
| This study | Rewetted peatland | mean ± 1 SD | 74 ± 18 | 1.2 ± 4.3 | -6 900 ± 5 600) | Peak growth season. Daytime. |
| This study | Lake littoral zone | mean ± 1 SD | 207 ± 19 | 8.6 ± 3.5 | -7 900 ± 5 800 | Peak growth season. Daytime. |

https://doi.org/10.5194/egusphere-2026-3826
Preprint. Discussion started: 17 August 2026


## Code and data availability

UAV-based data are available upon request from Magnus Gålfalk.

## Author contributions

Writing and editing: MG, DB, HS, GDG, ÅS. Data collection: MG, DB, HS, GDG. Methodology: MG, DB. Processing, analysis, software, and visualization: MG.

## Competing interests

The authors declare that they have no conflict of interest.

## Disclaimer

Copernicus Publications remains neutral with regard to jurisdictional claims made in the text, published maps, institutional affiliations, or any other geographical representation in this paper. While Copernicus Publications makes every effort to include appropriate place names, the final responsibility lies with the authors. Views expressed in the text are those of the authors and do not necessarily reflect the views of the publisher.

## Acknowledgements

This study has been made possible by the Swedish Infrastructure for Ecosystem Science (SITES), in this case at Skogaryd. SITES current funding (2023-2028) is through the Swedish Research Council grant number 2021-00164. We would also like to thank the project ”En handbok som visar hur vi bäst åtgärdar organogen mark från höga växthusgasemissioner till sänkor” (Formas grant no. 2019-01991).

https://doi.org/10.5194/egusphere-2026-3826
Preprint. Discussion started: 17 August 2026


**Financial support**

This project has received funding from the European Union's Horizon 2020 Research and Innovation Programme (Grant 101015825; TRIAGE), the Swedish Research Council VR (Grant VR 2022-03841), Knut and Alice Wallenberg Foundation (Grant no. KAW 2024.0034), and FORMAS (Grant 2022-01582).

**References**

Alvarez, R. A., Zavala-Araiza, D., Lyon, D. R., Allen, D. T., Barkley, Z. R., Brandt, A. R., Davis, K. J., Herndon, S. C., Jacob, D. J., Karion, A., Kort, E. A., Lamb, B. K., Lauvaux, T., Maasakkers, J. D., Marchese, A. J., Omara, M., Pacala, S. W., Peischl, J., Robinson, A. L., Shepson, P. B., Sweeney, C., Townsend-Small, A., Wofsy, S. C., and Hamburg, S. P.: Assessment of methane emissions from the U.S. oil and gas supply chain, Science, 361, 186–188, https://doi.org/10.1126/science.aar7204, 2018.

Basso, L. S., Marani, L., Gatti, L. V., Miller, J. B., Gloor, M., Melack, J., Cassol, H. L. G., Tejada, G., Domingues, L. G., Arai, E., Sanchez, A. H., Corrêa, S. M., Anderson, L., Aragão, L. E. O. C., Correia, C. S. C., Crispim, S. P., and Neves, R. A. L.: Amazon methane budget derived from multi-year airborne observations highlights regional variations in emissions, Commun Earth Environ, 2, 246, https://doi.org/10.1038/s43247-021-00314-4, 2021.

Bastviken, D. and Johnson, M. S.: Future methane emissions from lakes and reservoirs, Nat Water, 3, 1397–1410, https://doi.org/10.1038/s44221-025-00532-6, 2025.

Bastviken, D., Wilk, J., Duc, N. T., Gålfalk, M., Karlson, M., Neset, T.-S., Opach, T., Enrich-Prast, A., and Sundgren, I.: Critical method needs in measuring greenhouse gas fluxes, Environ. Res. Lett., 17, 104009, https://doi.org/10.1088/1748-9326/ac8fa9, 2022.

Bianchi, A., Larmola, T., Kekkonen, H., Saarnio, S., and Lång, K.: Review of Greenhouse Gas Emissions from Rewetted Agricultural Soils, Wetlands, 41, 108, https://doi.org/10.1007/s13157-021-01507-5, 2021.

Bolek, A., Heimann, M., and Göckede, M.: UAV-based in situ measurements of $CO_2$ and $CH_4$ fluxes over complex natural ecosystems, Atmos. Meas. Tech., 17, 5619–5636, https://doi.org/10.5194/amt-17-5619-2024, 2024.

Cao, M., Wang, F., Ma, S., Geng, H., and Sun, K.: Recent advances on greenhouse gas emissions from wetlands: Mechanism, global warming potential, and environmental drivers, Environmental Pollution, 355, 124204, https://doi.org/10.1016/j.envpol.2024.124204, 2024.

Corbett, A. and Smith, B.: A Study of a Miniature TDLAS System Onboard Two Unmanned Aircraft to Independently Quantify Methane Emissions from Oil and Gas Production Assets and Other Industrial Emitters, Atmosphere, 13, 804, https://doi.org/10.3390/atmos13050804, 2022.

https://doi.org/10.5194/egusphere-2026-3826
Preprint. Discussion started: 17 August 2026


Cossel, K. C., Waxman, E. M., Hoenig, E., Hesselius, D., Chaote, C., Coddington, I., and Newbury, N. R.: Ground-to-UAV, laser-based emissions quantification of methane and acetylene at long standoff distances, Atmos. Meas. Tech., 16, 5697–5707, https://doi.org/10.5194/amt-16-5697-2023, 2023.

Cottle, D. J., Nolan, J. V., and Wiedemann, S. G.: Ruminant enteric methane mitigation: a review, Animal Production Science, 51, 491–514, https://doi.org/10.1071/AN10163, 2011.

De Souza Maria, L., Rossi, F. S., Costa, L. M. D., Campos, M. O., Blas, J. C. G., Panosso, A. R., Silva, J. L. D., Silva Junior, C. A. D., and La Scala Jr, N.: Spatiotemporal analysis of atmospheric XCH4 as related to fires in the Amazon biome during 2015–2020, Remote Sensing Applications: Society and Environment, 30, 100967, https://doi.org/10.1016/j.rsase.2023.100967, 2023.

Dimitriadou, S., Kokkinos, P. A., Kyzas, G. Z., and Kalavrouziotis, I. K.: Fit-for-purpose WWTP unmanned aerial systems: A game changer towards an integrated and sustainable management strategy, Science of The Total Environment, 949, 174966, https://doi.org/10.1016/j.scitotenv.2024.174966, 2024.

Dooley, J. F., Minschwaner, K., Dubey, M. K., El Abbadi, S. H., Sherwin, E. D., Meyer, A. G., Follansbee, E., and Lee, J. E.: A New Technique for Airborne Measurements to Quantify Methane Emissions Over a Wide Range: Implementation and Validation, https://doi.org/10.5194/egusphere-2024-760, 19 March 2024.

Escobar, D., Belyazid, S., and Manzoni, S.: Back to the Future: Restoring Northern Drained Forested Peatlands for Climate Change Mitigation, Front. Environ. Sci., 10, 834371, https://doi.org/10.3389/fenvs.2022.834371, 2022.

Filkin, T., Lipin, I., and Sliusar, N.: Integrating a UAV System Based on Pixhawk with a Laser Methane Mini Detector to Study Methane Emissions, Drones, 7, 625, https://doi.org/10.3390/drones7100625, 2023.

Gålfalk, M. and Bastviken, D.: In Situ Observations Reveal Underestimated Greenhouse Gas Emissions from Wastewater Treatment with Anaerobic Digestion – Sludge Was a Major Source for Both $CH_4$ and $N_2O$, Environ. Sci. Technol., 59, 18146–18155, https://doi.org/10.1021/acs.est.5c04780, 2025.

Gålfalk, M., Nilsson Påledal, S., and Bastviken, D.: Sensitive Drone Mapping of Methane Emissions without the Need for Supplementary Ground-Based Measurements, ACS Earth Space Chem., 5, 2668–2676, https://doi.org/10.1021/acsearthspacechem.1c00106, 2021.

Gålfalk, M., Påledal, S. N., Sehlén, R., and Bastviken, D.: Ground-based remote sensing of CH4 and N2O fluxes from a wastewater treatment plant and nearby biogas production with discoveries of unexpected sources, Environmental Research, 204, 111978, https://doi.org/10.1016/j.envres.2021.111978, 2022.

Gatti, L. V., Basso, L. S., Miller, J. B., Gloor, M., Gatti Domingues, L., Cassol, H. L. G., Tejada, G., Aragão, L. E. O. C., Nobre, C., Peters, W., Marani, L., Arai, E., Sanches, A. H., Corrêa, S. M., Anderson, L., Von Randow, C., Correia, C. S. C., Crispim, S. P., and Neves, R. A. L.: Amazonia as a carbon source linked to deforestation and climate change, Nature, 595, 388–393, https://doi.org/10.1038/s41586-021-03629-6, 2021.

Han, T., Xie, C., Liu, Y., Yang, Y., Zhang, Y., Huang, Y., Gao, X., Zhang, X., Bao, F., and Li, S.-M.: Development of a continuous UAV-mounted air sampler and application to the quantification of $CO_2$ and $CH_4$ emissions from a major coking plant, Atmos. Meas. Tech., 17, 677–691, https://doi.org/10.5194/amt-17-677-2024, 2024.

Harper, L. A., Denmead, O. T., and Flesch, T. K.: Micrometeorological techniques for measurement of enteric greenhouse gas emissions, Animal Feed Science and Technology, 166–167, 227–239, https://doi.org/10.1016/j.anifeedsci.2011.04.013, 2011.

https://doi.org/10.5194/egusphere-2026-3826
Preprint. Discussion started: 17 August 2026


Hashim, M., Ng, H. L., Zakari, D. M., Sani, D. A., Chindo, M. M., Hassan, N., Azmy, M. M., and Pour, A. B.: Mapping of Greenhouse Gas Concentration in Peninsular Malaysia Industrial Areas Using Unmanned Aerial Vehicle-Based Sniffer Sensor, Remote Sensing, 15, 255, https://doi.org/10.3390/rs15010255, 2023.

Hollenbeck, D., Zulevic, D., and Chen, Y.: Advanced Leak Detection and Quantification of Methane Emissions Using sUAS, Drones, 5, 117, https://doi.org/10.3390/drones5040117, 2021.

IEA: Global Methane Tracker 2022, International Energy Agency, International Energy Agency, 2022.

Jońca, J., Pawnuk, M., Bezyk, Y., Arsen, A., and Sówka, I.: Drone-Assisted Monitoring of Atmospheric Pollution—A Comprehensive Review, Sustainability, 14, 11516, https://doi.org/10.3390/su141811516, 2022.

Kasimir Klemedtsson, Å., Lindgren, A., Tuorda, T. L., and Wingborg, J.: Torvmarker, klimat och återvätning: att minska utsläpp och främja koldioxidinlagring, Vulkan, Stockholm, 153 pp., 2024.

Kim, K. T., Kim, H., Jeong, S., Lee, Y. S., Choi, E., and Kim, J. Y.: Quantification of greenhouse gas emissions from a municipal solid waste incinerator using an uncrewed aerial vehicle, Environment International, 198, 109396, https://doi.org/10.1016/j.envint.2025.109396, 2025.

Koffi, E. N., Bergamaschi, P., Alkama, R., and Cescatti, A.: An observation-constrained assessment of the climate sensitivity and future trajectories of wetland methane emissions, Sci. Adv., 6, eaay4444, https://doi.org/10.1126/sciadv.aay4444, 2020.

Lauvaux, T., Giron, C., Mazzolini, M., d'Aspremont, A., Duren, R., Cusworth, D., Shindell, D., and Ciais, P.: Global assessment of oil and gas methane ultra-emitters, Science, 375, 557–561, https://doi.org/10.1126/science.abj4351, 2022.

Liengaard, L., Nielsen, L. P., Revsbech, N. P., Priemé, A., Elberling, B., Enrich-Prast, A., and Kühl, M.: Extreme Emission of N2O from Tropical Wetland Soil (Pantanal, South America), Front. Microbio., 3, https://doi.org/10.3389/fmicb.2012.00433, 2013.

Liu, W., Feng, X., Niu, Z., Zhou, W., Chen, H., Liang, D., Lyu, M., Wang, G., and Liu, L.: Temporal characteristics and vertical profiles of atmospheric CH4 at the northern foot of the Qinling Mountains in China, Atmospheric Environment, 337, 120786, https://doi.org/10.1016/j.atmosenv.2024.120786, 2024.

Liu, Y., Paris, J.-D., Vrekoussis, M., Antoniou, P., Constantinides, C., Desservettaz, M., Keleshis, C., Laurent, O., Leonidou, A., Philippon, C., Vouterakos, P., Quéhé, P.-Y., Bousquet, P., and Sciare, J.: Improvements of a low-cost $CO_2$ commercial nondispersive near-infrared (NDIR) sensor for unmanned aerial vehicle (UAV) atmospheric mapping applications, Atmos. Meas. Tech., 15, 4431–4442, https://doi.org/10.5194/amt-15-4431-2022, 2022.

Malerba, M. E., De Kluyver, T., Wright, N., Schuster, L., and Macreadie, P. I.: Methane emissions from agricultural ponds are underestimated in national greenhouse gas inventories, Commun Earth Environ, 3, 306, https://doi.org/10.1038/s43247-022-00638-9, 2022.

Milberg, P., Törnqvist, L., Westerberg, L. M., and Bastviken, D.: Temporal variations in methane emissions from emergent aquatic macrophytes in two boreonemoral lakes, AoB PLANTS, 9, https://doi.org/10.1093/aobpla/plx029, 2017.

Moore, D. P., Li, N. P., Wendt, L. P., Castañeda, S. R., Falinski, M. M., Zhu, J.-J., Song, C., Ren, Z. J., and Zondlo, M. A.: Underestimation of Sector-Wide Methane Emissions from United States Wastewater Treatment, Environ. Sci. Technol., 57, 4082–4090, https://doi.org/10.1021/acs.est.2c05373, 2023.

https://doi.org/10.5194/egusphere-2026-3826
Preprint. Discussion started: 17 August 2026


Moormann, L., Böttger, T., Schuhmann, P., Valero, L., Fachinger, F., and Drewnick, F.: The Flying Laboratory FLab: development and application of a UAS to measure aerosol particles and trace gases in the lower troposphere, Atmos. Meas. Tech., 18, 1441–1459, https://doi.org/10.5194/amt-18-1441-2025, 2025.

Myers, D. E.: Interpolation and estimation with spatially located data, Chemometrics and Intelligent Laboratory Systems, 11, 209–228, https://doi.org/10.1016/0169-7439(91)85001-6, 1991.

Olaguer, E., Jeltema, S., Gauthier, T., Jermalowicz, D., Ostaszewski, A., Batterman, S., Xia, T., Raneses, J., Kovalchick, M., Miller, S., Acevedo, J., Lamb, J., Benya, J., Wendling, A., and Zhu, J.: Landfill Emissions of Methane Inferred from Unmanned Aerial Vehicle and Mobile Ground Measurements, Atmosphere, 13, 983, https://doi.org/10.3390/atmos13060983, 2022.

Omara, M., Zavala-Araiza, D., Lyon, D. R., Hmiel, B., Roberts, K. A., and Hamburg, S. P.: Methane emissions from US low production oil and natural gas well sites, Nat Commun, 13, 2085, https://doi.org/10.1038/s41467-022-29709-3, 2022.

Rutherford, J. S., Sherwin, E. D., Ravikumar, A. P., Heath, G. A., Englander, J., Cooley, D., Lyon, D., Omara, M., Langfitt, Q., and Brandt, A. R.: Closing the methane gap in US oil and natural gas production emissions inventories, Nat Commun, 12, 4715, https://doi.org/10.1038/s41467-021-25017-4, 2021.

Scheller, J. H., Mastepanov, M., and Christensen, T. R.: Toward UAV-based methane emission mapping of Arctic terrestrial ecosystems, Science of The Total Environment, 819, 153161, https://doi.org/10.1016/j.scitotenv.2022.153161, 2022.

Scheutz, C., Knudsen, J. E., Vechi, N. T., and Knudsen, J.: Validation and demonstration of a drone-based method for quantifying fugitive methane emissions, Journal of Environmental Management, 373, 123467, https://doi.org/10.1016/j.jenvman.2024.123467, 2025.

Song, C., Zhu, J.-J., Willis, J. L., Moore, D. P., Zondlo, M. A., and Ren, Z. J.: Methane Emissions from Municipal Wastewater Collection and Treatment Systems, Environ. Sci. Technol., 57, 2248–2261, https://doi.org/10.1021/acs.est.2c04388, 2023.

Soskind, M. G., Li, N. P., Moore, D. P., Chen, Y., Wendt, L. P., McSpiritt, J., Zondlo, M. A., and Wysocki, G.: Stationary and drone-assisted methane plume localization with dispersion spectroscopy, Remote Sensing of Environment, 289, 113513, https://doi.org/10.1016/j.rse.2023.113513, 2023.

Tassielli, G., Cananà, L., and Spalatro, M.: Detection of Methane Leaks via a Drone-Based System for Sustainable Landfills and Oil and Gas Facilities: Effect of Different Variables on the Background-Noise Measurement, Sustainability, 16, 7748, https://doi.org/10.3390/su16177748, 2024.

Van Hove, A., Aalstad, K., Lind, V., Arndt, C., Odongo, V., Ceriani, R., Fava, F., Hulth, J., and Pirk, N.: Inferring methane emissions from African livestock by fusing drone, tower, and satellite data, Biogeosciences, 22, 4163–4186, https://doi.org/10.5194/bg-22-4163-2025, 2025.

Wang, J., Xia, X., Liu, S., Zhang, S., Dong, J., Wang, G., Xu, W., Zhang, L., Zheng, W., Zhang, Z., Chen, X., Yuan, L., Liu, J., Zhang, J., Xin, Y., McDowell, W. H., Tian, H., Bastviken, D., and Yang, Z.: Globally doubled methane emissions from nutrient-enriched rivers, National Science Review, 13, nwag192, https://doi.org/10.1093/nsr/nwag192, 2026.

Wang, Y., Guo, X., Huo, Y., Li, M., Pan, Y., Yu, S., Baklanov, A., Rosenfeld, D., Seinfeld, J. H., and Li, P.: Toward a versatile spaceborne architecture for immediate monitoring of the global methane pledge, Atmos. Chem. Phys., 23, 5233–5249, https://doi.org/10.5194/acp-23-5233-2023, 2023.

https://doi.org/10.5194/egusphere-2026-3826
Preprint. Discussion started: 17 August 2026


Wietzel, J. B. and Schmidt, M.: Methane emission mapping and quantification in two medium-sized cities in Germany: Heidelberg and Schwetzingen, Atmospheric Environment: X, 20, 100228, https://doi.org/10.1016/j.aeaoa.2023.100228, 2023.

Wilson, T. C., Brenner, J., Morrison, Z., Jacob, J. D., and Elbing, B. R.: Wind Speed Statistics from a Small UAS and Its Sensitivity to Sensor Location, Atmosphere, 13, 443, https://doi.org/10.3390/atmos13030443, 2022.

Yong, H., Allen, G., Mcquilkin, J., Ricketts, H., and Shaw, J. T.: Lessons learned from a UAV survey and methane emissions calculation at a UK landfill, Waste Management, 180, 47–54, https://doi.org/10.1016/j.wasman.2024.03.025, 2024.

Zhu, Z., González-Rocha, J., Ding, Y., Frausto-Vicencio, I., Heerah, S., Venkatram, A., Dubey, M., Collins, D., and Hopkins, F. M.: Toward on-demand measurements of greenhouse gas emissions using an uncrewed aircraft AirCore system, Atmos. Meas. Tech., 17, 3883–3895, https://doi.org/10.5194/amt-17-3883-2024, 2024.